Escola de Camins
Escola Tècnica Superior d'Enginyeria de Camins, Canals i Ports
UPC BARCELONATECH

Evaluación de la técnica acoplada de elementos finitos y elementos discretos en problemas de fractura de rocas. Aplicación a voladuras en frentes de túneles

TREBALL FINAL DE MÀSTER

Treball realitzat per:
Alejandro Cornejo Velázquez

Dirigit per:

José Francisco Zárate Araiza
Eugenio Oñate Ibáñez de Navarra

Màster en:
Enginyeria de Camins, Canals i Ports

Barcelona, 14/06/2017

Departament de Resistència de Materials i Estructures

Numerical Simulation of Multi-Fracture in Materials Using a Coupled FEM-DEM Formulation

Alejandro Cornejo Velázquez

Escola Tècnica Superior d'Enginyers de Camins, Canals i Ports de Barcelona
Universitat Politècnica de Catalunya

Master Thesis

Advisors:
Prof. Eugenio Oñate
Prof. Francisco Zárate

June 2017

Numerical simulation of multi-fracture in materials using a coupled FEM-DEM formulation.

April 2017
Universitat Politècnica de Catalunya
c/ Jordi Girona 1-3, 08034 Barcelona
www.upc.edu

Agradecimientos

A medida que avanzaba en la realización de esta tesina, me he dado cuenta de la cantidad de conocimientos que he podido ir adquiriendo así como la experiencia ganada a base de cometer errores e intentar superarlos continuamente. Dicha tarea hubiera sido mucho más difícil sin el apoyo de mis dos tutores, Eugenio Oñate y Francisco Zárate, los cuales me introdujeron la temática de la tesina y me ayudaron en todos los problemas que fueron aconteciendo. También debo agradecerles el hecho de brindarme la oportunidad de trabajar con grandes investigadores de CIMNE que, sin duda, me han ayudado en gran medida tanto en el ámbito técnico como en el personal.

En este sentido quiero expresar mi más sincero agradecimiento a Lucia Gratiela Barbu y Miguel Ángel Celigueta por su infinita paciencia y comprensión, a ellos les debo gran parte de mi evolución como ingeniero y, sin duda, como persona.

No podría terminar este apartado sin mencionar a mi familia, a ellos les debo el haber llegado hasta aquí. Concretamente querría agradecer a mi madre su apoyo y cariño incondicional así como su gran habilidad dando consejos sobre culquier tema. A mi padre por valorar mis avances y apoyar cualquier decisión. A mi hermano, por siempre estar allí en todo momento y siempre pasar momentos divertidos y, por último, a mi pareja Laura, por acompañarme en mis horas de estudio y redacción de este documento.

También quiero agradecer su paciencia y sincera amistad a Adrián, Dani y Christian, gracias por escucharme y darme consejos cuando los necesitaba.

Por último, quiero acordarme de mis compañeros de CIMNE que me han ayudado en muchas de mis tareas y que, en un corto espacio de tiempo, me han hecho sentir como en casa. Entre ellos quiero destacar a Sergio Oller y Alex H. Barbat, los cuales me han enseñado mucho sobre nuestra profesión y a Cuauhtemoc Escudero, por ser un excelente compañero de despacho y amigo.

Resumen

El objetivo de la presente tesis es evaluar la eficiencia de un nuevo método numérico que acopla el conocido método de elementos finitos (MEF) con el método de elementos discretos (DEM) para la predicción de las multi-fracturas que se producen en los materiales sometidos a un estado de cargas determinado. Se expondrán también las ventajas de emplear la tecnología FEM-DEM en detrimento de otras formulaciones ya existentes como el método de elementos discretos (DEM) o los modelos de daño convencionales.

La tecnología FEM-DEM se comporta inicialmente como un modelo de daño, que considera que el comportamiento no-lineal inelástico que sufre un sólido cohesivo-friccional es consecuencia de la formación y desarrollo de micro-fisuras. Una vez se alcanza un cierto nivel de deterioro del material, la formulación FEM-DEM sustituye ese elemento carente de rigidez por elementos discretos que seguirán la evolución de la fractura. Es por este motivo que se le denomina teoría FEM-DEM ya que se parte de una geometría inicial de elementos finitos, los cuales van a ser solicitados por unas cargas exteriores y, según la intensidad de las mismas, van a deteriorarse hasta transfigurarse en elementos discretos.

En primera instancia se ha aplicado dicha técnica al estudio de la rotura de probetas de rocas sometidas a ensayos de compresión uniaxial, tracción indirecta y ensayo de corte. Los ejemplos anteriores fueron de vital importancia para realizar una primera validación del código empleado. A continuación se ha estudiado la aplicación de la técnica FEM-DEM al estudio de la fractura de un frente de túnel sometido a una secuenciación de cargas de voladura determinada así como la simulación de un arco de mampostería sometido a un asiento diferencial.

Abstract

The objective of this thesis is to evaluate the efficiency of a new numerical technique that couples the well known finite element method (FEM) with the discrete element method (DEM) in order to predict the onset and evolution of fractures in a continuum subjected to a loading system. Additionally, will be exposed the advantages of using the FEM-DEM theory rather than other existing formulations such as the DEM or the classic damage models.

The FEM-DEM formulation initially behaves as a damage model. These models consider that the non-linear behaviour of a cohesive-frictional material is directly related to the creation and propagation of micro-fractures inside the continuum. Once a finite element surpasses a certain level of damage, the FEM-DEM formulation removes that finite element and the discrete elements are generated at the nodes of the damaged element. It is for this reason that the formulation is named FEM-DEM, the model defines the initial geometry with finite elements which are going to be loaded and, according to the stress level, removed and substituted with discrete elements.

Firstly, the FEM-DEM has been used to simulate the behaviour of rock samples subjected to uni-axial, indirect tensile and shear tests. The previous examples were of central importance to validate the code and ensure its correctness.

Finally, two examples related to civil/mining methods were performed, a tunnel portal subjected to a sequential blast loading and a masonry arch with a differential settlement.

Contents

List of Figures

List of Tables

Chapter 1

Introduction and objectives

In the recent years extensive research has been conducted in order to simulate de onset and propagation of fractures within a continuous medium. In the field of the finite element method there are some procedures for crack prediction in frictional materials. However, these procedures are often very complex and require to remesh in the vicinity of the micro-fractures as well as the application of incremental-iterative strategies based on the arc-length control in order to be efficient [4],[10], [21].

Furthermore, the discrete element method (DEM) [7], [14], [28], [24], [26], [25], [27], [37] has shown a fairly good qualitatively results. However, the inherent difficulty for calibrating the mechanical properties of the material , as well as the requirement for a huge number of discrete elements to cover a large scale geometry mitigate its effectiveness.

The numerical technique proposed in this thesis uses the FEM to model de continuum and simulates the opening of fractures through the generation of the DEM once the fully damaged element is removed. The method extends a well defined crack opening methodology termed Element Elimination Technique (EET) [13], [22], [34] that creates discrete elements at the crack lips. The onset of a fracture is conditioned by a single parameter (yield stress) damage model whose evolution is governed by the fracture energy. As stated above, once the damage of an element surpass a certain threshold, that element is removed from the finite element mesh and the generation of discrete elements is carried out.

Therefore, the objective of this work is to validate the FEM-DEM formulation briefly described above. This verification involves the creation of several numerical

simulations and its calculation trough the FEM-DEM code and, in some cases, with another validated codes in order to compare the results. In other cases the validation is done by means of analytical solutions when possible. In this context, classical uni-axial compression test and indirect tensile test were performed as well as simple beam calculations, earth dams, tunnel portals subjected to blast loading and so on.

The thesis is organized as follows. First of all, a brief introduction to the finite element method is explained, with particular emphasis on the damage models used in FEM and its intrinsic non-linearity and the procedures to solve this kind of problems.

In the third chapter is briefly described the mentioned discrete element method (DEM), whose understanding is crucial to follow the FEM-DEM formulation. Afterwards, the FEM-DEM formulation is widely described in the case of 2D and 3D geometry.

Finally, some of the numerical simulations in 2D and 3D are shown using different finite element meshes to ensure a well performance of the code.

Chapter 2

Damage Mechanics with FEM

In this paragraph the most relevant features about the FEM which serve a base to the damage models are presented. Afterwards the damage mechanics are described. These damage models are of central importance because it is the way that the FEM-DEM formulation realises that the finite element is fully damaged and has to be removed, with the consequent generation of discrete elements.

2.1 Introduction to the Finite Element Method

Most engineering structures are continuum, and so their behaviour cannot be properly represented in terms of a few number of discrete variables. A rigorous analysis of such structures requires the integration of the differential equations that govern the equilibrium of a generic differential element belonging to them.

Although a continuous structure is inherently three-dimensional (3D), its behaviour can be accurately described in some cases by one- (1D) or two-dimensional (2D) structural models. This occurs, for instance, in the analysis of plates in bending, where only the deformation of the plate mid-plane is considered. Other examples are the structures modelled as 2D solids or as axisymmetric solids (i.e. dams, tunnels, water tanks, etc.)

The Finite Element Method (FEM) is a numerical technique for finding approximate solutions to boundary value problems for partial differential equations. It uses subdivisions of a whole problem domain, and variational methods to solve the problem by minimizing an associated error function. In the end, FEM connects many simple element equations over many small domains, to approximate a more complex equation over a larger domain. The integration of partial differential equations helps the engineer to study uni, bi and three-dimensional structural problems, including its time evolution. In order to correctly perform a simulation with the finite element method, it is advisable to follow the next steps:

- *Step 1:* Starting with the geometrical description of the problem, knowing the boundary conditions and the applied loads, one must to select a structural model that is going to simulate the structure. The material properties must also be defined, as well as the scope of the analysis (small or large displacements, static or dynamic analysis,etc.).
- *Step 2:* The structure is subdivided into a mesh of non-intersecting domains termed finite elements (*discretization process*). The problem variables (displacements) are interpolated within each element in terms of their values at a known set of points of the element called *nodes*.
- *Step 3:* From the Principle of Virtual Work one can obtain the stiffness matrices $K^{(e)}$ and the load vectors $f^{(e)}$ for each element.
- *Step 4:* The element stiffness and the load terms are assembled into the overall stiffness matrix K and the load vector f for the structure.
- *Step 5:* The global system of linear simultaneous equations $Ka = f$ is solved for the unknown displacement variables a.
- *Step 6:* Once the displacements a are computed, the strains and the stresses are evaluated within each element. Reactions at the nodes restrained against movement are also computed.
- *Step 7:* After a successful computer run, the next step is the interpretation and presentation of results. Results are presented graphically to aid their interpretation and checking (*post-processing step*).
- *Step 8:* Having assessed the finite element results, the analyst may consider several modifications which may be introduced at various stages of the analysis. For example, it may be found that the structural model selected is inappropriate and hence it should be adequately modified.

Can be concluded that the FEM is a very powerful technique to obtain approximate solutions for structural problems. However, being an approximate method

it involves a certain error in the numerical values and users should always look upon FEM results with a critical eye.

Since the FEM-DEM formulation has been implemented in 2D and 3D, the two formulations are going to be presented in the following paragraphs.

2.1.1 Two Dimensional Elasticity Theory

This chapter initiates the application of the FEM to structures which satisfy the assumptions of two-dimensional (2D) elasticity (i.e. plane stress or plane strain). Many of the concepts here studied will be useful when dealing with other structural problems in the subsequent chapters. Therefore, this chapter is introductory to the application of the FEM to continuous 2D and 3D structures.

There are a wide number of structures of practical interest which can be analyzed following the assumptions of 2D elasticity. All these structures have a sort of prismatic geometry. Depending on the relative dimensions of the prism and the loading type, the following two categories can be distinguished:

- *Plane stress problems:* A prismatic structure is under plane stress if one of its dimensions (thickness) is much smaller than the other two and all the loads are contained in the middle plane of the structure. The analysis domain is the middle section (Fig. 4.1). Amongst the structural problems that can be included in the plane stress category we find the analysis of deep beams, plates and walls under in-plane loading, buttress dams, etc.(Fig. 2.1).
- *Plane strain problems:* A prismatic structure is under plane strain if one of its dimensions (length) is larger than the other two and all the loads are uniformly distributed along its length and they act orthogonally to the longitudinal axis. The analysis domain is a cross section to this axis (Fig. 4.2). Amongst the structures which follow the plane strain assumption we find containing walls, gravity dams, pressurised pipes and many problems of geotechnical engineering (tunnels, foundations, etc.)(Fig. 2.2).

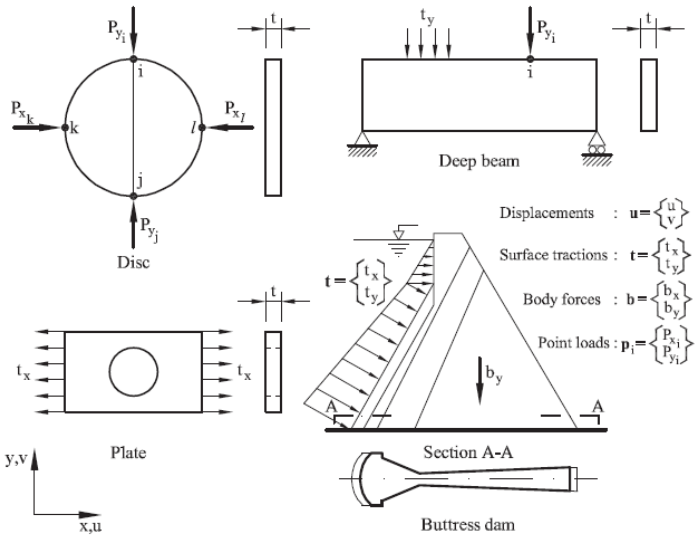

Figure 2.1: Examples of plane stress problems [23]

Next, we present the concepts of 2D elasticity theory needed for the application of the FEM.

2.1.1.1 Displacements, strains and stresses fields

Both the plane stress and plane strain assumptions imply that the transversal sections to the prismatic axis z deform in the same manner and also that the displacement along the z axis is negligible. Therefore, only a generic 2D transverse section in the plane $x-y$ needs to considered for the analysis. Thereby, the vector of displacements at any point is defined as:

$$\mathbf{u}(x,y) = \begin{Bmatrix} u(x,y) \\ v(x,y) \end{Bmatrix} \tag{2.1}$$

where $u(x,y)$ and $v(x,y)$ are the displacements of an arbitrary point in the directions x and y, respectively.

The displacement field (2.1) allows the corresponding strains to be derived from standard elasticity theory [36] as follows:

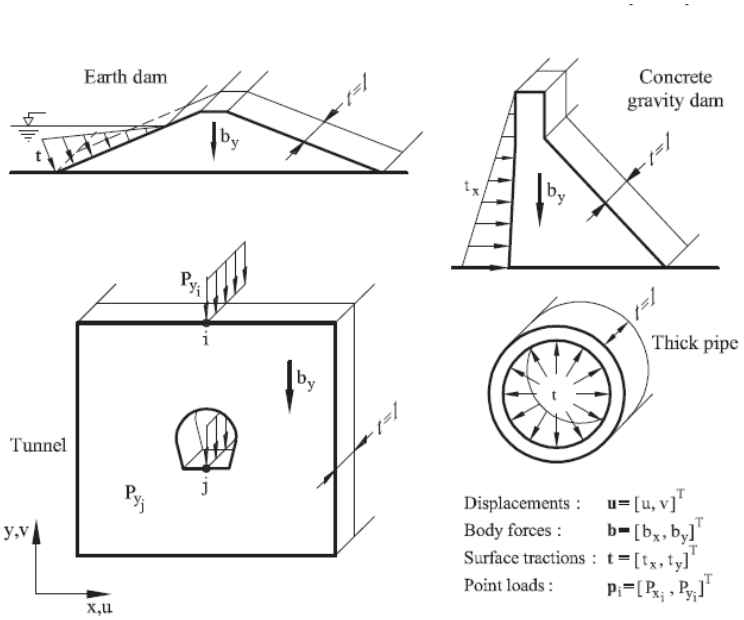

Figure 2.2: Examples of plane strain problems [23]

$$\begin{aligned} \varepsilon_x &= \frac{\partial u}{\partial x} \\ \varepsilon_y &= \frac{\partial v}{\partial y} \\ \gamma_{xy} &= \frac{\partial u}{\partial y} + \frac{\partial v}{\partial x} \\ \gamma_{xz} &= \gamma_{yz} = 0 \end{aligned} \tag{2.2}$$

The longitudinal strain ε_z is negligible in the plane strain case. Furthermore, in the case of plane stress the ε_z is not zero but the conjugate stress σ_z can be ignored. The point these theories have in common is that the work performed $(\varepsilon_z \cdot \sigma_z)$by the longitudinal strain has to be zero. Consequently, the *strain vector* is defined in both cases simply as:

$$\boldsymbol{\varepsilon} = \begin{bmatrix} \varepsilon_x & \varepsilon_y & \gamma_{xy} \end{bmatrix}^T \tag{2.3}$$

Following the reasoning stated in the Eq. (2.3), we can assume that the stress components τ_{xz} and τ_{yz} are zero. For the same reasons of the previous paragraph, the stress field can defined as follows.

$$\boldsymbol{\sigma} = \begin{bmatrix} \sigma_x & \sigma_y & \tau_{xy} \end{bmatrix}^T \tag{2.4}$$

Once the strain and stress vector have been presented, it is important to know

the relation between them. This relationship is derived from the 3D elasticity theory. After applying the previously stated hypothesis into the three-dimensional constitutive equation of elasticity we obtain the stress-strain relationship [36].

$$\boldsymbol{\sigma} = \boldsymbol{D}\boldsymbol{\varepsilon} \tag{2.5}$$

where D is the elastic material matrix (or constitutive matrix)

$$\mathbf{D} = \begin{bmatrix} d_{11} & d_{12} & 0 \\ d_{21} & d_{22} & 0 \\ 0 & 0 & d_{33} \end{bmatrix} \tag{2.6}$$

For isotropic elasticity we have

$$\begin{array}{ll} \text{Plane stress} & \text{Plane strain} \\ d_{11} = d_{22} = \dfrac{E}{1-\nu^2} & d_{11} = d_{22} = \dfrac{E(1-\nu)}{(1+\nu)(1-2\nu)} \\ d_{12} = d_{21} = \nu d_{11} & d_{12} = d_{21} = d_{11}\dfrac{\nu}{1-\nu} \\ d_{33} = \dfrac{E}{2(1+\nu)} = G & d_{33} = \dfrac{E}{2(1+\nu)} = G \end{array} \tag{2.7}$$

With E being the Young's modulus and ν the poisson's ratio.

2.1.1.2 Virtual work principle

The PVW has the following expression for the 2D elasticity problems.

$$\int\int_A (\delta\varepsilon_x\sigma_x + \delta\varepsilon_y\sigma_y + \delta\gamma_{xy}\tau_{xy})tdA = \int\int_A (\delta u b_x + \delta v b_y)tdA + \int_s (\delta u t_x + \delta v t_y)tds + \sum_i (\delta u_i P_{x_i} + \delta v_i P_{x_i}) \tag{2.8}$$

The terms in the right hand side (RHS) of the equation represent the virtual work of the body forces (b_x and b_y), the surface tractions (t_x and t_y) and the external point loads (P_{x_i} and P_{x_i}). Furthermore, the terms in the left hand side (LHS) represent the virtual work of the internal forces in the continuum.

2.1.1.3 Three-noded triangular element

Since the FEM-DEM formulation in the 2D problems uses the simple 3-noded element it is justified to focus on this kind of finite element. Additionally, the simplicity of the 3-noded element allows an easy the assimilation of the FEM, which is also the objective of this paragraph.

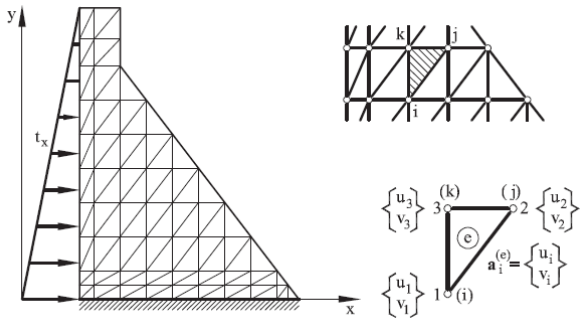

Figure 2.3: Triangular 3 noded element discretization example [23]

Conversely, it has limited accuracy due to the linear displacement approximation yielding constant strain and stress fields. Hence, fine meshes are required to capture accurate solutions in zones of high displacement gradients. This problem is solved generating an adaptative mesh refinement in order to enhance the quality of the results.

2.1.1.4 Discretization of the displacements, strains and stresses fields

If we consider a single triangular element like that shown in the Fig. 2.3, the two Cartesian displacements of an arbitrary point within the element can be expressed in terms of the nodal displacements as follows.

$$\begin{aligned} u &= N_1 u_1 + N_2 u_2 + N_3 u_3 \\ v &= N_1 v_1 + N_2 v_2 + N_3 v_3 \end{aligned} \tag{2.9}$$

Where u_i and v_i are the horizontal and vertical displacements respectively and the N_i are the so called *shape functions*. These shape functions are the functions which interpolates the solution between the discrete values obtained at the mesh nodes. Therefore, appropriate functions have to be used and, as already mentioned, low order polynomials are typically chosen as shape functions.

The equation (2.9) can be written as

$$\mathbf{u} = \begin{bmatrix} N_1 & 0 & N_2 & 0 & N_3 & 0 \\ 0 & N_1 & 0 & N_2 & 0 & N_3 \end{bmatrix} \begin{Bmatrix} u_1 \\ v_1 \\ u_2 \\ v_2 \\ u_3 \\ v_3 \end{Bmatrix} \tag{2.10}$$

or

$$\mathbf{u} = \mathbf{N}\mathbf{a}^{(e)} \tag{2.11}$$

where

$$\mathbf{N} = \begin{bmatrix} \mathbf{N}_1 & \mathbf{N}_2 & \mathbf{N}_3 \end{bmatrix}; \mathbf{N}_i = \begin{bmatrix} N_i & 0 \\ 0 & N_i \end{bmatrix} \tag{2.12}$$

are the shape function matrices of the element at the ith node and

$$\mathbf{a}^{(e)} = \begin{Bmatrix} \mathbf{a}_1 \\ \mathbf{a}_2 \\ \mathbf{a}_3 \end{Bmatrix}; \mathbf{a}_i^{(e)} = \begin{Bmatrix} u_i \\ v_i \end{Bmatrix} \tag{2.13}$$

are the nodal displacements of the node i. The linear shape functions mentioned before have the expression shown in the Eq. (2.14).

$$N_i = \frac{1}{2A^{(e)}}(a_i + xb_i + yc_i) \tag{2.14}$$

where

$$a_i = x_j y_k - x_k y_j \qquad b_i = y_j - y_k \qquad c_i = x_k - x_j \qquad i,j,k = 1,2,3 \tag{2.15}$$

It can be checked that the shape function N_i takes the value one at node i and zero at the other two nodes. Applying the same discretization to the strain field:

$$\begin{aligned} \varepsilon_x &= \frac{\partial u}{\partial x} = \frac{\partial N_1}{\partial x}u_1 + \frac{\partial N_2}{\partial x}u_2 + \frac{\partial N_3}{\partial x}u_3 \\ \varepsilon_y &= \frac{\partial v}{\partial y} = \frac{\partial N_1}{\partial y}v_1 + \frac{\partial N_2}{\partial y}u_2 + \frac{\partial N_3}{\partial y}v_3 \\ \gamma_{xy} &= \frac{\partial u}{\partial y} + \frac{\partial v}{\partial x} = \frac{\partial N_1}{\partial y}u_1 + \frac{\partial N_1}{\partial x}v_1 + \frac{\partial N_2}{\partial y}u_2 + \frac{\partial N_2}{\partial x}v_2 + \frac{\partial N_3}{\partial y}u_3 + \frac{\partial N_3}{\partial x}v_3 \end{aligned} \tag{2.16}$$

The Eq. (2.16) can be rewritten in matrix form as:

$$\boldsymbol{\varepsilon} = \begin{Bmatrix} \dfrac{\partial u}{\partial x} \\ \dfrac{\partial v}{\partial y} \\ \dfrac{\partial u}{\partial y} + \dfrac{\partial v}{\partial x} \end{Bmatrix} = \left[\begin{array}{cc:cc:cc} \dfrac{\partial N_1}{\partial x} & 0 & \dfrac{\partial N_2}{\partial x} & 0 & \dfrac{\partial N_3}{\partial x} & 0 \\ 0 & \dfrac{\partial N_1}{\partial y} & 0 & \dfrac{\partial N_2}{\partial y} & 0 & \dfrac{\partial N_3}{\partial y} \\ \dfrac{\partial N_1}{\partial y} & \dfrac{\partial N_1}{\partial x} & \dfrac{\partial N_2}{\partial y} & \dfrac{\partial N_2}{\partial x} & \dfrac{\partial N_3}{\partial y} & \dfrac{\partial N_3}{\partial x} \end{array}\right] \begin{Bmatrix} u_1 \\ v_1 \\ u_2 \\ v_2 \\ u_3 \\ v_3 \end{Bmatrix} \tag{2.17}$$

or

$$\boldsymbol{\varepsilon} = \mathbf{B}\mathbf{a}^{(e)} \tag{2.18}$$

where

$$\mathbf{B} = \begin{bmatrix} \mathbf{B}_1 & \mathbf{B}_2 & \mathbf{B}_3 \end{bmatrix} \tag{2.19}$$

is the element strain matrix, and

$$\mathbf{B}_i = \begin{bmatrix} \dfrac{\partial N_i}{\partial x} & 0 \\ 0 & \dfrac{\partial N_i}{\partial y} \\ \dfrac{\partial N_i}{\partial y} & \dfrac{\partial N_i}{\partial x} \end{bmatrix} \tag{2.20}$$

is the strain matrix of the node i.

The discretized expression of the stress field within the element is obtained by substituting the Eq. (2.18) into the Eq. (2.5) as

$$\boldsymbol{\sigma} = \mathbf{D}\boldsymbol{\varepsilon} = \mathbf{D}\mathbf{B}\mathbf{a}^{(e)} \tag{2.21}$$

If initial strains and stresses are considered

$$\boldsymbol{\sigma} = \mathbf{D}(\boldsymbol{\varepsilon} - \boldsymbol{\varepsilon}^0) + \boldsymbol{\sigma}^0 \tag{2.22}$$

where the $\boldsymbol{\varepsilon}^0$ are the initial strains vector. For the case of initial strains due to thermal effects ans isotropic material, the initial strain vector has the following expressions

$$\begin{array}{cc} \text{Plane stress} & \text{Plane strain} \\ \boldsymbol{\varepsilon}^0 = \begin{Bmatrix} \alpha\Delta T \\ \alpha\Delta T \\ 0 \end{Bmatrix} & \boldsymbol{\varepsilon}^0 = (1+\nu)\begin{Bmatrix} \alpha\Delta T \\ \alpha\Delta T \\ 0 \end{Bmatrix} \end{array} \tag{2.23}$$

Note that the shape functions of the 3-noded triangular element are linear polynomials. This implies that the derivatives of the shape functions are going to be constant so the strain and stress vector are going to be constant within the element. Therefore, a finer mesh will be needed in zones where stress gradients are higher, so that the strain and stress fields are accurately approximated.

2.1.1.5 Discretized equilibrium equations

The discretized equilibrium equations for the 3-noded triangle will be derived by applying the PVW to an individual element.

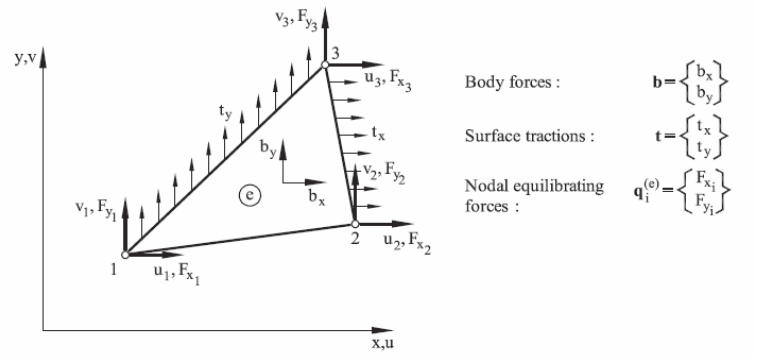

Figure 2.4: External forces acting on an element [23]

As we can see in the Fig. 2.4, the acting forces on an element can be:

- Distributed forces **b** per unit area (body forces)
- Distributed forces **t** per unit length (surface tractions)
- Nodal equilibrating forces **q**

If we rewrite the Eq. (2.8) in matrix form:

$$\int\int_A \delta\boldsymbol{\varepsilon}^T \boldsymbol{\sigma} t dA = \int\int_A \delta\mathbf{u}^T \mathbf{b} t dA + \oint_l \delta\mathbf{u}^T \mathbf{t} t ds + \sum_{i=1}^{3} (\delta u_i F_{x_i} + \delta v_i F_{x_i}) \quad (2.24)$$

where δu_i and δv_i are the nodal virtual displacements and F_{x_i} and F_{y_i} the equilibrating nodal forces along the horizontal and vertical directions,respectively. Next we interpolate the virtual displacements in terms of the nodal values. Following the same procedure as for deriving the Eqs. (2.11) and (2.18) we obtain

$$\delta\mathbf{u} = \mathbf{N}\delta\mathbf{a}^{(e)} \qquad \delta\boldsymbol{\varepsilon} = \mathbf{B}\delta\mathbf{a}^{(e)} \quad (2.25)$$

Substituting the last Eq. into (2.24) gives:

$$[\delta\mathbf{a}^{(e)}]^T \left[\int\int_{A^{(e)}} \mathbf{B}^T \boldsymbol{\sigma} t dA - \int\int_{A^{(e)}} \mathbf{N}^T \mathbf{b} t dA - \oint_{l_{(e)}} \mathbf{N}^T \mathbf{t} t da \right] = [\delta\mathbf{a}^{(e)}]^T \mathbf{q}^{(e)} \quad (2.26)$$

Since the virtual displacements are arbitrary it is deduced that

$$\int\int_{A^{(e)}} \mathbf{B}^T \boldsymbol{\sigma} t dA - \int\int_{A^{(e)}} \mathbf{N}^T \mathbf{b} t dA - \oint_{l_{(e)}} \mathbf{N}^T \mathbf{t} t da = \mathbf{q}^{(e)} \tag{2.27}$$

Substituting the stresses in terms of the nodal displacements from the Eq. (2.21) gives

$$\int\int_{A^{(e)}} \mathbf{B}^T (\boldsymbol{D}\boldsymbol{B}\boldsymbol{a}^{(e)} - \boldsymbol{D}\boldsymbol{\varepsilon}^0 + \boldsymbol{\sigma}^0) t dA - \int\int_{A^{(e)}} \mathbf{N}^T \mathbf{b} t dA - \oint_{l_{(e)}} \mathbf{N}^T \mathbf{t} t da = \mathbf{q}^{(e)} \tag{2.28}$$

so

$$\int\int_{A^{(e)}} \mathbf{B}^T \boldsymbol{D}\boldsymbol{B} t dA \mathbf{a}^{(e)} - \int\int_{A^{(e)}} \mathbf{B}^T \boldsymbol{D}\boldsymbol{\varepsilon}^0 t dA + \int\int_{A^{(e)}} \mathbf{B}^T \boldsymbol{\sigma}^0 t dA - \int\int_{A^{(e)}} \mathbf{N}^T \mathbf{b} t dA - \oint_{l_{(e)}} \mathbf{N}^T \mathbf{t} t da = \mathbf{q}^{(e)} \tag{2.29}$$

or

$$\mathbf{K}^{(e)} \mathbf{a}^{(e)} - \mathbf{f}^{(e)} = \mathbf{q}^{(e)} \tag{2.30}$$

where

$$\mathbf{K}^{(e)} = \int\int_{A^{(e)}} \mathbf{B}^T \mathbf{D} \mathbf{B} t dA \tag{2.31}$$

is the elemental **stiffness matrix**, and

$$\mathbf{f}^{(e)} = \mathbf{f}_{\varepsilon}^{(e)} + \mathbf{f}_{\sigma}^{(e)} + \mathbf{f}_{b}^{(e)} + \mathbf{f}_{t}^{(e)} \tag{2.32}$$

is the equivalent **nodal force vector** where

$$\mathbf{f}_{\varepsilon}^{(e)} = \int\int_{A^{(e)}} \mathbf{B}^T \boldsymbol{D}\boldsymbol{\varepsilon}^0 t dA \tag{2.33}$$

$$\mathbf{f}_{\sigma}^{(e)} = -\int\int_{A^{(e)}} \mathbf{B}^T \boldsymbol{\sigma}^0 t dA \tag{2.34}$$

$$\mathbf{f}_{b}^{(e)} = \int\int_{A^{(e)}} \mathbf{N}^T \mathbf{b} t dA \tag{2.35}$$

$$\mathbf{f}_{t}^{(e)} = \oint_{l_{(e)}} \mathbf{N}^T \mathbf{t} t da \tag{2.36}$$

are the equivalent nodal force vectors due to initial strains, initial stresses, body forces and surface tractions, respectively. It is important to remark that the expressions of the element stiffness matrix and the equivalent nodal force vector are completely general and compatible with 2D solid element.

Therefore, the global equilibrium equation of the mesh can be obtained by assembling the contributions of stiffness matrices and vectors of equivalent nodal forces of the different elements. The global matrix equation can be written like:

$$\mathbf{Ka} = \mathbf{f} \tag{2.37}$$

where $\mathbf{K}$, $\mathbf{a}$ and $\mathbf{f}$ are, respectively, the stiffness matrix, the vector of nodal displacements, and the vector of equivalent nodal forces of the whole mesh.

The assembly process is schematically described in the Fig. 2.5.

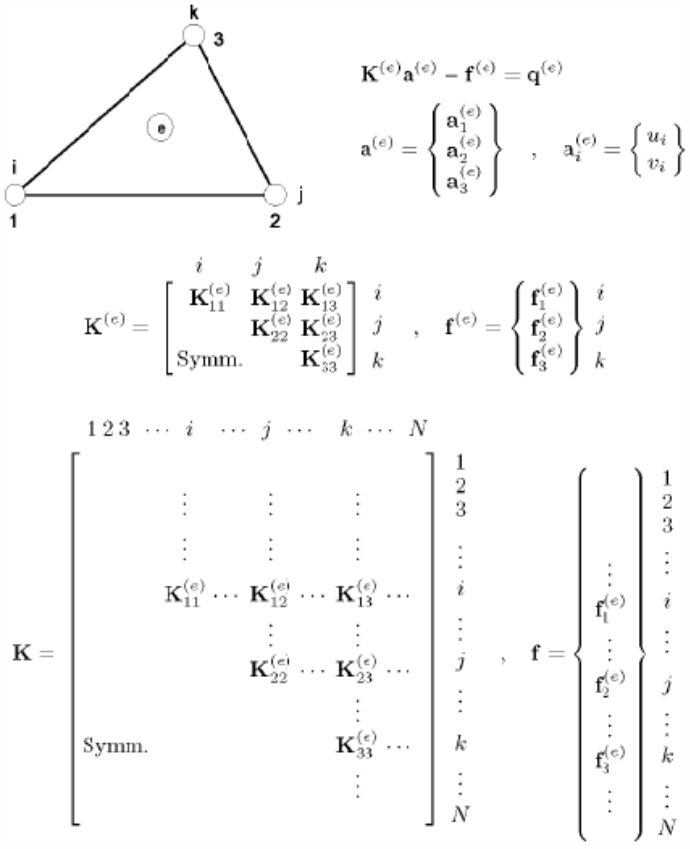

Figure 2.5: Assembly of the stiffness matrix and the equivalent nodal force vector into the global system for the 3-noded triangle with node numbers i,j,k [23]

We note once more that the equilibrating nodal forces due to the surface tractions along the element interface cancel themselves out during the assembly process.

Therefore, only the surface tractions acting on element sides belonging to the external boundaries of the structure must be considered in the analysis. The reactions at the prescribed nodes are computed a "posteriori" using the Eq. (2.30).

2.1.1.6 Shape functions for C^0 continuous triangular elements

The shape functions for the more popular C^0 continuous triangular elements are complete polynomials whose terms can be readily identified by the Pascal triangle. This also defines the position of the nodes within the element. In order to obtain the shape functions of high order elements it is usually used the the technique based on area coordinates that is explained below.

Area coordinates

Let us join a point P within a triangle of area A with the three vertices 1, 2, 3 (Fig. 2.6). This defines three sub-areas inside the element (A_1,A_2 and A_3)whose sum has to be the total area. The area coordinates are defined as

$$L_1 = \frac{A_1}{A} \qquad L_2 = \frac{A_2}{A} \qquad L_3 = \frac{A_3}{A} \tag{2.38}$$

with

$$L_1 + L_2 + L_3 = 1 \tag{2.39}$$

The position of point P can be defined by any two of these three coordinates. The area coordinates of a node can be interpreted as the ratio between the distance from point P to the opposite side divided by the distance from the node to that side. In the FEM context area coordinates have proved to be very useful for deriving the shape functions of triangular finite elements.

Area coordinates are also of interest to define a parametric interpolation of the element geometry. For a straight side triangle the following relationship between the area and the Cartesian coordinates can be written:

$$\begin{aligned} x &= L_1 x_1 + L_2 x_2 + L_3 x_3 \\ y &= L_1 y_1 + L_2 y_2 + L_3 y_3 \end{aligned} \tag{2.40}$$

Using the Eq. (2.40) and completing the system with (2.39) can be obtained

$$L_i = \frac{1}{2A^{(e)}}(a_i + b_i x + c_i y) \tag{2.41}$$

with $A^{(e)}$ being the area of the element and a_i, b_i, c_i coincide with the values given in the Eq. (2.15).

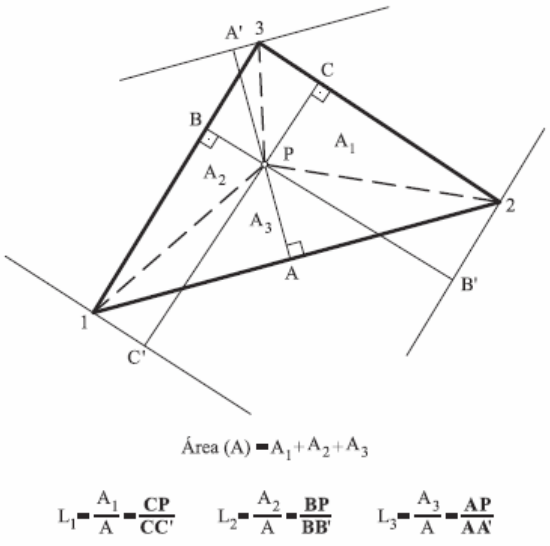

Figure 2.6: Area coordinates for a triangle [23]

Derivation of the shape functions for C^0 continuous triangles

The shape functions for triangles containing complete Mth degree polynomials can be obtained in terms of the area coordinates as follows. Let us consider a node i characterized by the position (I, J, K) where I, J and K are the powers of the area coordinates L_1, L_2 and L_3, respectively in the expression of the shape function. Thus, $I + J + K = M$ and the shape function of node i is given by

$$N_i = l_I^i(L_1) l_J^i(L_2) l_K^i(L_3) \tag{2.42}$$

where $l_I^i(L_1)$ is the normalized 1D Lagrange Ith degree polynomial in L_1 which takes value one at the node i, i.e.

$$l_I^i(L_1) = \prod_{j=1, I+1, j\neq i} \frac{(L_1 - L_1^j)}{(L_1^i - L_1^j)} \tag{2.43}$$

where L_1^i is the value of L_1 at node i with identical expressions for $l_J^i(L_2)$ and $l_K^i(L_3)$.

The values of I, J, K for each node can be deduced from the Fig. 2.7.

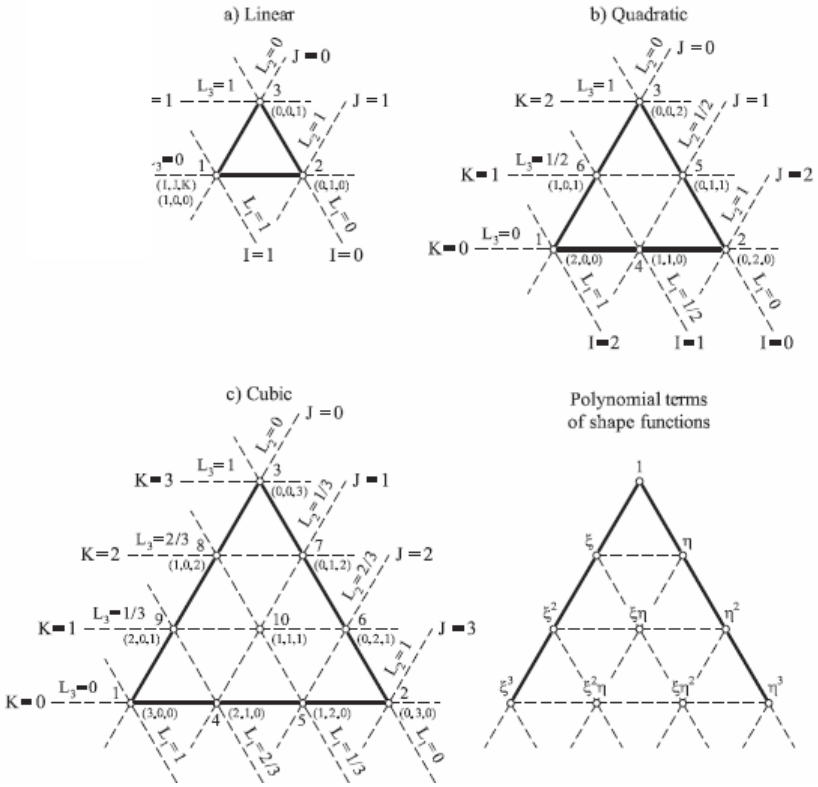

Figure 2.7: Area coordinates and values of (I,J,K) for each node [23]

Natural coordinates for triangles

It is convenient to define a normalized coordinate system α, β (also called natural coordinate system), such that the triangle has the sides over the lines $\alpha = 0, \beta = 0$ and $1 - \alpha - \beta = 0$.

These coincidences allow us to express the shape functions of triangular elements in terms of the natural coordinates. This is particularly useful for deriving isoparametric triangular elements.

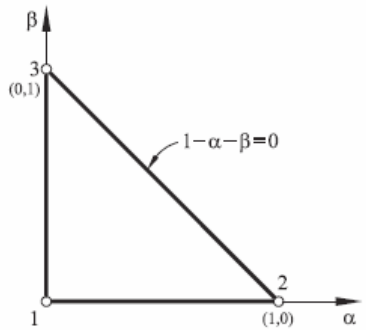

Figure 2.8: Natural coordinates for a triangular element [23]

2.1.1.7 Isoparametric 2D solid elements and numerical integration

Up to now we have described how to obtain the shape functions for 2D solid elements of triangular shape and how to compute the stiffness matrix and the equivalent nodal force vector for straight sided triangular elements.

Consequently, the derivation of 2D solid elements of arbitrary shape using *isoparametric formulation* and *numerical integration* is explained.

The integration of the expressions of the stiffness matrix and the vectors of equivalent nodal forces, will be performed by means of Gauss-Legendre quadratures. This technique allow us to integrate any function over a normalized domain, using tabulated Gauss point coordinates and weights. However, we need to transform first the integrals over the element domain into integrals over the normalized space of the natural coordinates. The concept of isoparametric interpolation comes from the usage of the same shape functions to interpolate the geometry and the displacements.

$$x = \sum_{i=1}^{n} N_i(\alpha, \beta) x_i \qquad\qquad y = \sum_{i=1}^{n} N_i(\alpha, \beta) y_i \tag{2.44}$$

where $N_i(\alpha, \beta)$ are the element shape functions. The Eqs. (2.44) relate the cartesian coordinates with the natural coordinates α and β.

If we assume that $N_i(\alpha,\beta) = N_i(x(\alpha,\beta), y(\alpha,\beta))$:

$$\begin{aligned}\frac{\partial N_i}{\partial \alpha} &= \frac{\partial N_i}{\partial x}\frac{\partial x}{\partial \alpha} + \frac{\partial N_i}{\partial y}\frac{\partial y}{\partial \alpha} \\ \frac{\partial N_i}{\partial \beta} &= \frac{\partial N_i}{\partial x}\frac{\partial x}{\partial \beta} + \frac{\partial N_i}{\partial y}\frac{\partial y}{\partial \beta}\end{aligned} \tag{2.45}$$

In matrix format:

$$\begin{Bmatrix} \frac{\partial N_i}{\partial \alpha} \\ \\ \frac{\partial N_i}{\partial \beta} \end{Bmatrix} = \begin{bmatrix} \frac{\partial x}{\partial \alpha} & \frac{\partial y}{\partial \alpha} \\ \\ \frac{\partial x}{\partial \beta} & \frac{\partial y}{\partial \beta} \end{bmatrix} \begin{Bmatrix} \frac{\partial N_i}{\partial x} \\ \\ \frac{\partial N_i}{\partial y} \end{Bmatrix} = \mathbf{J}^{(e)} \begin{Bmatrix} \frac{\partial N_i}{\partial x} \\ \\ \frac{\partial N_i}{\partial y} \end{Bmatrix} \tag{2.46}$$

where $\mathbf{J}^{(e)}$ is the Jacobian matrix of the transformation of natural coordinates to the Cartesian ones. From (2.46) we can derive:

$$\begin{Bmatrix} \frac{\partial N_i}{\partial x} \\ \\ \frac{\partial N_i}{\partial y} \end{Bmatrix} = [\mathbf{J}^{(e)}]^{-1} \begin{Bmatrix} \frac{\partial N_i}{\partial \alpha} \\ \\ \frac{\partial N_i}{\partial \beta} \end{Bmatrix} = \frac{1}{\det \mathbf{J}^{(e)}} \begin{bmatrix} \frac{\partial y}{\partial \beta} & -\frac{\partial y}{\partial \alpha} \\ \\ -\frac{\partial x}{\partial \beta} & \frac{\partial x}{\partial \alpha} \end{bmatrix} \begin{Bmatrix} \frac{\partial N_i}{\partial \alpha} \\ \\ \frac{\partial N_i}{\partial \beta} \end{Bmatrix} \tag{2.47}$$

where $\det(\mathbf{J}^{(e)})$ is the determinant of the Jacobian matrix. In this context, the relationship between the differential of area is

$$dxdy = \det(\mathbf{J}^{(e)}) d\alpha d\beta \tag{2.48}$$

Now, using the isoparametric transformation (2.44) we can derive the terms of the Jacobian:

$$\frac{\partial x}{\partial \xi} = \sum_{i=1}^{n} \frac{\partial N_i}{\partial \xi} x_i \qquad \frac{\partial x}{\partial \eta} = \sum_{i=1}^{n} \frac{\partial N_i}{\partial \eta} x_i \qquad etc. \tag{2.49}$$

and so:

$$\mathbf{J}^{(e)} = \sum_{i=1}^{n} \begin{bmatrix} \frac{\partial N_i}{\partial \xi} x_i & \frac{\partial N_i}{\partial \xi} y_i \\ \\ \frac{\partial N_i}{\partial \eta} x_i & \frac{\partial N_i}{\partial \eta} y_i \end{bmatrix} \tag{2.50}$$

Applying the Eq. (2.50) for a 3-noded triangular element we obtain:

$$\mathbf{J}^{(e)} = \begin{bmatrix} x_2 - x_1 & y_2 - y_1 \\ x_3 - x_1 & y_3 - y_1 \end{bmatrix}^{(e)} \tag{2.51}$$

Now the integrals in the elements stiffness matrix are transformed to the normalized natural coordinate space as

$$\mathbf{K}_{ij}^{(e)} = \int\int_{A^{(e)}} \mathbf{B}_i^T \mathbf{D} \mathbf{B}_j t dx dy = \int_0^1 \int_0^{1-\beta} \mathbf{B}_i^T(\alpha,\beta) \mathbf{D} \mathbf{B}_j(\alpha,\beta) \det(\mathbf{J}^{(e)})^{-1} t d\alpha d\beta \tag{2.52}$$

By now, all the necessary theory about the transformation between the two systems of coordinates (original and the isoparametric) have been presented. In this context, the numerical integration by a Gauss quadrature will be explained. In order to remind the procedure of integration using the Gauss quadratures, two examples of integration over rectangular and triangular domains are shown.

The integration of a generic function $f(\xi, \eta)$ over the domain of natural coordinates of a quadrilateral element can be evaluated by means of a Gauss quadrature like:

$$\int_{-1}^{1}\int_{-1}^{1} f(\xi,\eta)d\xi d\eta = \int_{-1}^{1} d\xi \left[\sum_{q=1}^{n_q} f(\xi,\eta_p)W_q\right] = \sum_{q=1}^{n_q}\sum_{p=1}^{n_p} f(\xi_q,\eta_p)W_qW_p \quad (2.53)$$

where n_p and n_q are the number of integration points in each direction ξ and η; ξ_p and η_q are the natural coordinates of the integration points p and q and W_p and W_q are the integration weights.

On the other hand, the Gauss quadrature for a triangular element can be written like:

$$\int_{0}^{1}\int_{0}^{1-\beta} f(\alpha,\beta)d\alpha d\beta = \sum_{p=1}^{n_p} f(\alpha_p,\beta_p)W_p \quad (2.54)$$

where n_p is the number of integration points: α_p and β_p are the isoparametric coordinates (area coordinates if the element has straight sides) and the corresponding weight for the pth integration point.

The coordinates and weights of the integration points are tabulated. And the number of integration points must be properly chosen tankig into account that the numerical quadrature of order n obtains an exact integral of polynomials of order $< 2n-1$ in the corresponding natural coordinate.

Applying the Gauss quadratures to the computation of the integrals involved in the Stiffness matrices of triangular elements we obtain:

$$\mathbf{K}_{ij}^{(e)} = \int_{0}^{1}\int_{1}^{1-\beta} \mathbf{B}_i^T\mathbf{D}\mathbf{B}_j t dx dy = \sum_{p=1}^{n_p}\left[\mathbf{B}_i^T\mathbf{D}\mathbf{B}_j \det\mathbf{J}^{(e)}\right]_p W_p t \quad (2.55)$$

Thereby, we can see that the numerical integration of the stiffness matrix requires the evaluation of the Jacobian $\mathbf{J}^{(e)}$, its determinant $\det(J^{(e)})$, the deformation matrix $\mathbf{B}$, the constitutive matrix $\mathbf{D}$, and the thickness t at each integration point.

2.1.2 Three Dimensional Elasticity Overview

Since the FEM-DEM formulation is available to perform 3D simulations, a brief introduction (not so detailed as in 2D) to the 3D elasticity must be carried out. Many structures have geometrical, mechanical or loading features which make it impossible to use the simple plane stress/plane strain models studied the previous chapter. The only alternative is to perform a full three dimensional (3D) analysis based on general 3D elasticity theory.

Examples of these situations are found in solids with irregular shapes and in the study of prismatic solids with heterogeneous material properties or arbitrary loading (see Fig. 2.72). Despite its apparent complexity, the analysis of a 3D solid with the FEM does not introduce major conceptual problems. 3D elasticity theory is a straightforward extension of the 2D case and the steps involved in the 3D finite element analysis of a structure are a repetition of those studied in the previous chapter. In that respect, this chapter closes the cycle of structural problems which can be analyzed using elasticity theory, either by the general 3D form or by any of the simplified 2D cases previously studied.

Although conceptually simple, 3D finite element computations involve a considerable amount of work in comparison with 2D analyses. The principal reason is the introduction of an additional space dimension, for this leads to greater computational time as well as requiring more effort to input data and visualize the results.

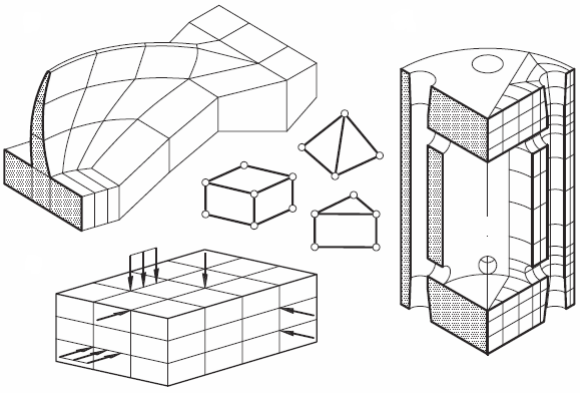

Figure 2.9: Structures which require a 3D analysis [23]

2.1.2.1 Displacements, strains and stresses fields

If we analyse a 3D solid (see Fig. 2.72), the movement of a point is defined by three components of the displacement vector, i.e.

$$\mathbf{u} = \left[u, v, w\right]^T \tag{2.56}$$

where *u,v,w* are the displacements of the point in the directions of the cartesian axes *x,y,z*, respectively. The strain field is defined by the standard six strain components of 3D elasticity. The strain vector is written as

$$\boldsymbol{\varepsilon} = \left[\varepsilon_x, \varepsilon_y, \varepsilon_z, \gamma_{xy}, \gamma_{xz}, \gamma_{yz}\right]^T \tag{2.57}$$

with

$$\varepsilon_x = \frac{\partial u}{\partial x} \qquad \varepsilon_y = \frac{\partial v}{\partial y} \qquad \varepsilon_z = \frac{\partial w}{\partial z} \tag{2.58}$$

$$\gamma_{xy} = \frac{\partial u}{\partial y} + \frac{\partial v}{\partial x} \qquad \gamma_{xz} = \frac{\partial u}{\partial z} + \frac{\partial w}{\partial x} \qquad \gamma_{yz} = \frac{\partial v}{\partial z} + \frac{\partial w}{\partial y}$$

Analogously, the stress field is defined by the six stress components which are conjugate of the six non-zero strains of Eq.(2.58). The stress vector is

$$\boldsymbol{\sigma} = \left[\sigma_x, \sigma_y, \sigma_z, \tau_{xy}, \tau_{xz}, \tau_{yz}\right]^T \tag{2.59}$$

Isotropic materials require two material parameters only, the Young modulus E and the Poisson's ratio ν. The constitutive matrix for isotropic materials can be directly written in global cartesian axes. If initial strains and stresses are taken into account we can write

$$\boldsymbol{\sigma} = \mathbf{D}(\boldsymbol{\varepsilon} - \boldsymbol{\varepsilon}^0) + \boldsymbol{\sigma}^0 \tag{2.60}$$

where the isotropic constitutive matrix $\mathbf{D}$ is given by

$$\mathbf{D} = \Xi \begin{bmatrix} 1 & \frac{\nu}{1-\nu} & \frac{\nu}{1-\nu} & 0 & 0 & 0 \\ & 1 & \frac{\nu}{1-\nu} & 0 & 0 & 0 \\ & & 1 & 0 & 0 & 0 \\ & & & \frac{1-2\nu}{2(1-\nu)} & 0 & 0 \\ & & & & \frac{1-2\nu}{2(1-\nu)} & 0 \\ Symmetrical & & & & & \frac{1-2\nu}{2(1-\nu)} \end{bmatrix} \tag{2.61}$$

where $\Xi = \dfrac{E(1-\nu)}{(1+\nu)(1-2\nu)}$.

The initial strain vector due to thermal strains is

$$\boldsymbol{\varepsilon}^0 = \alpha(\Delta T)[1,1,1,0,0,0]^T \tag{2.62}$$

2.1.2.2 3D Virtual work principle

The expression of the Virtual work principle for 3D solids is

$$\int\int\int_V \delta\boldsymbol{\varepsilon}^T \boldsymbol{\sigma} dV \;=\; \int\int\int_V \delta\mathbf{u}^T \mathbf{b} dV + \int\int_A \delta\mathbf{u}^T \mathbf{t} dA + \sum_{i=1}(\delta\mathbf{a}_i \mathbf{F}_i) \tag{2.63}$$

where V and A are respectively the volume and the surface of the solid over which the body forces $\mathbf{b} = [b_x, b_y, b_z]^T$ and the surface tractions $\mathbf{t} = [t_x, t_y, t_z]^T$ act, and $\mathbf{F}_i = [F_{x_i}, F_{y_i}, F_{z_i}]^T$ are the point loads acting at node i.

2.1.2.3 The four-noded tetrahedron

Since the FEM-DEM formulation uses the four-noded tetrahedron when 3D computations are corried out, it is justified to focus on this element. It is important to note that most of the expressions are general and applicable to any 3D element with n nodes.

2.1.2.4 Discretization of the displacement field

If we consider a 3D solid discretized into 4-noded tetrahedra as that of Fig. 2.10, the displacement field within each element is interpolated as

$$\mathbf{u} = \begin{Bmatrix} u \\ v \\ w \end{Bmatrix} = \begin{Bmatrix} N_1 u_1 + N_2 u_2 + N_3 u_3 + N_4 u_4 \\ N_1 v_1 + N_2 v_2 + N_3 v_3 + N_4 v_4 \\ N_1 w_1 + N_2 w_2 + N_3 w_3 + N_4 w_4 \end{Bmatrix} = \sum_{i=1}^{4} \mathbf{N}_i \mathbf{a}_i^{(e)} = \mathbf{N}\mathbf{a}^{(e)} \quad (2.64)$$

where

$$\mathbf{N} = [\mathbf{N}_1, \mathbf{N}_2, \mathbf{N}_3, \mathbf{N}_4] \qquad \mathbf{N}_i = \begin{bmatrix} N_i & 0 & 0 \\ 0 & N_i & 0 \\ 0 & 0 & N_i \end{bmatrix} \quad (2.65)$$

and

$$\mathbf{a}^{(e)} = \begin{Bmatrix} \mathbf{a}_1^{(e)} \\ \mathbf{a}_2^{(e)} \\ \mathbf{a}_3^{(e)} \\ \mathbf{a}_4^{(e)} \end{Bmatrix} \qquad \mathbf{a}_i^{(e)} = \begin{Bmatrix} u_i \\ v_i \\ w_i \end{Bmatrix} \quad (2.66)$$

are the shape function matrix and the displacement vector for the element and a node i, respectively. As usual, the same interpolation has been used for the three displacement components. The shape functions are therefore the same for the three displacements.

The analytical form of the shape functions Ni is obtained in a similar way as for the 3-noded triangle. The four nodes define a linear displacement field in 3D. The nodal shape function N_i is obtained using the following expression:

$$N_i = \frac{1}{6V^{(e)}}(a_i + b_i x + c_i y + d_i z) \quad (2.67)$$

where $V^{(e)}$ is the element volume and

$$a_i = \det \begin{bmatrix} x_j & y_j & z_j \\ x_k & y_k & z_k \\ x_l & y_l & z_l \end{bmatrix} \qquad b_i = -\det \begin{bmatrix} 1 & y_j & z_j \\ 1 & y_k & z_k \\ 1 & y_l & z_l \end{bmatrix} \quad (2.68)$$

$$c_i = \det \begin{bmatrix} x_j & 1 & z_j \\ x_k & 1 & z_k \\ x_l & 1 & z_l \end{bmatrix} \qquad d_i = -\det \begin{bmatrix} x_j & y_j & 1 \\ x_k & y_k & 1 \\ x_l & y_l & 1 \end{bmatrix}$$

The different parameters for $i = 1, 2, 3, 4$, are obtained by adequate cyclic permutation of the indexes i, j, k, l.

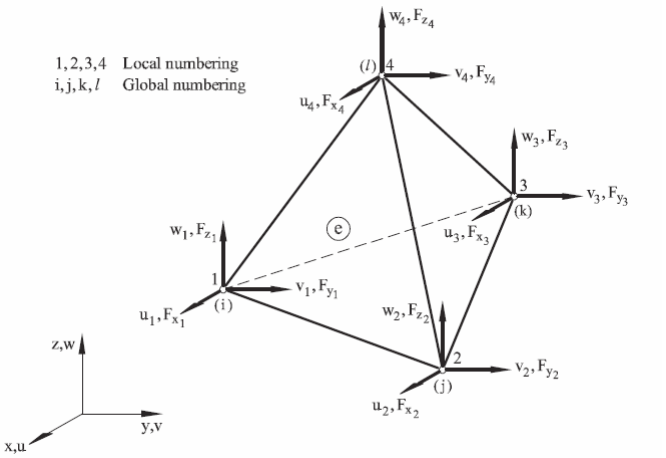

Figure 2.10: Four-noded tetrahedral element. Nodal displacements $(u_i; v_i; w_i)$ *and equilibrating nodal forces* $(F_{x_i}, F_{y_i}, F_{z_i})$ *[23]*

2.1.2.5 Strain matrix

Substituting the Eq. (2.64) into Eq. (2.58) gives for a 3D element with n nodes

$$\boldsymbol{\varepsilon} = \sum_{i=1}^{n} \begin{Bmatrix} \frac{\partial N_i}{\partial x} u_i \\ \frac{\partial N_i}{\partial y} v_i \\ \frac{\partial N_i}{\partial z} w_i \\ \frac{\partial N_i}{\partial y} u_i + \frac{\partial N_i}{\partial x} v_i \\ \frac{\partial N_i}{\partial z} u_i + \frac{\partial N_i}{\partial x} w_i \\ \frac{\partial N_i}{\partial z} v_i + \frac{\partial N_i}{\partial y} w_i \end{Bmatrix} = \sum_{i=1}^{n} \mathbf{B}_i \mathbf{a}_i^{(e)} = \mathbf{B}\mathbf{a}^{(e)} \tag{2.69}$$

where $\mathbf{B}$ is the element strain matrix given by

$$\mathbf{B} = [\mathbf{B}_1, \mathbf{B}_2, \mathbf{B}_3, \mathbf{B}_4] \tag{2.70}$$

end $\mathbf{B}_i$ is the strain matrix of the node i, with

$$\mathbf{B}_i = \begin{bmatrix} \frac{\partial N_i}{\partial x} & 0 & 0 \\ 0 & \frac{\partial N_i}{\partial y} & 0 \\ 0 & 0 & \frac{\partial N_i}{\partial z} \\ \frac{\partial N_i}{\partial y} & \frac{\partial N_i}{\partial x} & 0 \\ \frac{\partial N_i}{\partial z} & 0 & \frac{\partial N_i}{\partial x} \\ 0 & \frac{\partial N_i}{\partial z} & \frac{\partial N_i}{\partial y} \end{bmatrix} \tag{2.71}$$

Since the shape functions are linear polynomials, the strain matrix is constant along the element, as it happens with the linear triangle in the 2D elasticity.

2.1.2.6 Equilibrium equations

The virtual displacements and the virtual strains are interpolated in terms of the virtual displacement values in the standard form, i.e.

$$\delta\mathbf{u} = \mathbf{N}\delta\mathbf{a} \qquad\qquad \delta\boldsymbol{\varepsilon} = \mathbf{B}\delta\mathbf{a} \tag{2.72}$$

Substituting the Eq. (2.72) into the Eq. (2.63) can be obtained:

$$\int\int\int_V \boldsymbol{B}^T\boldsymbol{\sigma}dV = \int\int\int_V \mathbf{N}^T\mathbf{b}dV + \int\int_A \mathbf{N}^T\mathbf{t}dA + \mathbf{q}^{(e)} \tag{2.73}$$

Substituting the constitutive equation (Eq. 2.60) for the stresses into the previous expression gives the equilibrium equation for the element in the standard matrix form

$$\begin{aligned}\left(\int\int\int_V \boldsymbol{B}^T\boldsymbol{D}\boldsymbol{B}dV\right)\mathbf{a}^{(e)} - \int\int\int_V \boldsymbol{B}^T\boldsymbol{D}\boldsymbol{\varepsilon}^0 dV + \\ + \int\int\int_V \boldsymbol{B}^T\boldsymbol{\sigma}^0 dV - \int\int\int_V \mathbf{N}^T\mathbf{b}dV - \int\int_A \mathbf{N}^T\mathbf{t}dA = \mathbf{q}^{(e)}\end{aligned} \tag{2.74}$$

or

$$\mathbf{K}^{(e)}\mathbf{a}^{(e)} - \mathbf{f}^{(e)} = \mathbf{q}^{(e)} \tag{2.75}$$

The global system of equations $\mathbf{Ka} = \mathbf{f}$ is obtained by assembling the contributions of $\mathbf{K}^{(e)}$ and $\mathbf{f}^{(e)}$ for each element in the usual manner.

The 4-noded tetrahedron behaves similarly to the 3-noded linear triangle presented in the chapter 2.1.1.3.The element has a good ability to model uniform stress fields. However, its accuracy is poor for bending dominated problems, as well as in the presence of high stress gradients and finer meshes are needed in these zones.

2.2 Damage Mechanics

Continuum damage mechanics is a branch of continuum mechanics that describes the progressive loss of material integrity due to the propagation and coalescence of micro-cracks, micro-voids, and similar defects. These changes in the microstructure lead to an irreversible material degradation, characterized by a loss of stiffness that can be observed on the macro-scale.

The continuous damage theory was first introduced by Kachanov [12] in 1958 dealing with yield problems but it was accepted afterwards as a valid alternative for behaviour simulation of different materials and further developed by Rabotnov [33], Hayhurst [9], and Leckie and Hayhurst [15]. Thermodynamic formalism involved in the irreversible process of damage was developed by Lemaitre and Chaboche [16], and other important contributions to our knowledge about damage mechanics include: Mazars [19], Mazars and Pijaudier-Cabot [20], Simo and Ju [35], Oller and Oñate [32], etc.

During the last years the constitutive models known as continuous damage models have been widely accepted for the simulation of the complex constitutive behaviour of many materials used in engineering. These models are characterized by their simplicity in their implementation, versatility and coherence, as they are based on the continuous damage mechanics.

2.2.1 Uni-axial Damage Theory

In order to introduce the basics of the damage models, it is advisable to start with the uni-axial stress case. In this case the material is assumed as a bundle of fibers parallel to the loading direction (as shown in the Fig. 2.11). Initially, all

the fibers behave elastically and the loading is resisted by the total section of the material (S). Once the stress increases, some of the fibers start breaking and the cross section is directly reduced. In order to simplify the example, each fiber is assumed to be perfectly brittle. This means that once the maximum stress level is achieved, it drops to zero simulating the sudden failure of that fiber.

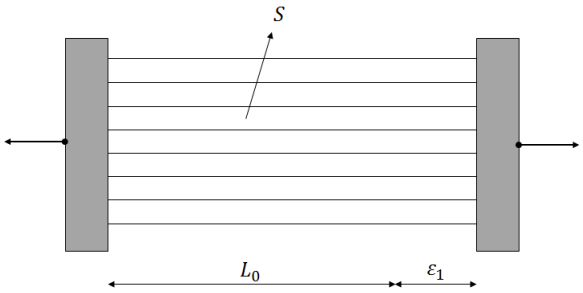

Figure 2.11: Idealized material with uniaxial loading

However, since the maximum stress level can differ from one fiber to another, the effective area $\overline{S}$ (the area corresponding to the resisting fibers) will decrease from $\overline{S} = S$ to $\overline{S} = 0$. Obviously, if the stress reduces, the remaining undamaged area is maintained.

It is important to distinguish between the *nominal stress* σ, defined as the force per unit initial area, and the *effective stress* $\overline{\sigma}$ defined as the force per unit effective area. The effective stress is the "actual" stress acting in the material micro structure. Since is known that $\sigma S = \overline{\sigma}\overline{S}$:

$$\sigma = \frac{\overline{S}}{S}\overline{\sigma} \tag{2.76}$$

It can be seen that the ratio $\overline{S}/S$ describes the integrity or degradation of the material. Thereby, we can define the damage parameter d as:

$$d = 1 - \frac{\overline{S}}{S} = \frac{S - \overline{S}}{S} = \frac{S_d}{S} \tag{2.77}$$

where S_d is the undamaged part of the area. The schematic process of degradation is shown in the Fig. 2.12.

The process shown in the Figs. 2.11 and 2.12 can be represented as a stress-strain curve as described in the Fig. 2.13.

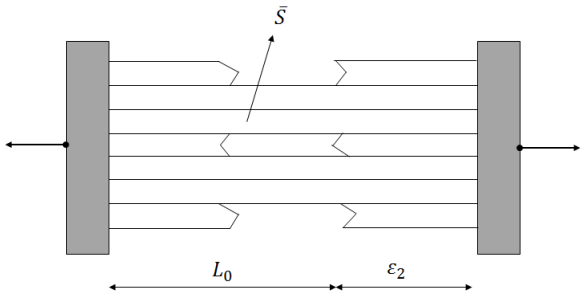

Figure 2.12: Idealized damaged material

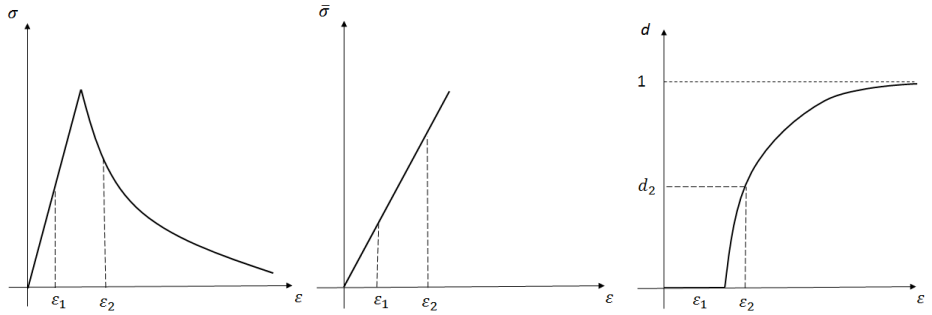

Figure 2.13: Stress-Strain curve ; Effective stress-strain curve ; Damage-strain curve

As can be seen in the Fig. 2.13, once the damage is different from zero, the maximum stress σ is reduced representing the so-called *softening*. Due to propagation of micro-defects and their coalescence, the damage variable grows and at the late stages of degradation process it approaches asymptotically the limit value $d = 1$, corresponding to a complete damaged material with effective stress reduced to zero.

As stated before, each fiber is supposed to behave as an elastic material until the maximum stress is achieved. Consequently, the *effective stress* $\overline{\sigma}$ is related to the strain of the material ε by:

$$\overline{\sigma} = D\varepsilon \tag{2.78}$$

where D is the elastic modulus of the undamaged material. If we combine the Eq. (2.76) and (2.78) it is easy to obtain the constitutive law for the nominal stress σ, that takes the form:

$$\sigma = (1 - d)D\varepsilon \tag{2.79}$$

In order to complete the described 1D model, it is necessary to define the evolution of the damage according to the strain level:

$$d = g(\varepsilon) \qquad 0 \leqslant d \leqslant 1 \tag{2.80}$$

The function g defines the shape of the stress-strain diagram and can be identified from an uni-axial test. In this context, we can introduce another function ψ that identifies whether the material is in elastic or plastic regime (flow rule). This function can be defined in this case as $\psi(\varepsilon, \varepsilon_{max}) = \varepsilon - \varepsilon_{max}$ where ε_{max} is the strain corresponding to the peak stress shown in the Fig. 2.13. This function also defines the elastic domain which is $\Omega_{elastic} = \{\varepsilon | \psi(\varepsilon, \varepsilon_{max}) < 0\}$.

The behaviour of the material and its variables remain elastic until the maximum stress level shown in the Fig. 2.13. This evolution of the effective stress is valid for a monotonic increasing load (ε). If the material is deformed up to a certain strain level ε_2, which induces its corresponding damage $g(\varepsilon_2)$, and the the strain reduces, the damaged area remains constant and the material responds as an elastic material with a reduced Young's modulus $D_2 = (1 - g(\varepsilon_2))D$. This means that the Young's modulus depends on the maximum reached strain and not on the current strain ε. This effect is shown in the Fig. 2.14.

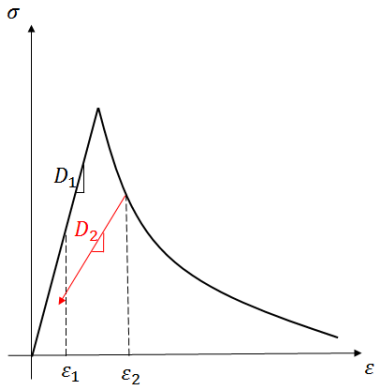

Figure 2.14: Uniaxial damage model through a non-monotonic loading

The consitutive law (Eq. (2.79)) can be rewritten as $\sigma = D_{sec}\varepsilon$ where D_{sec} is the secant or damaged modulus of elasticity.
At this point, the principal components of a damage model can be summarized as:

- The stress-strain law in secant format $\sigma = D_{sec}\varepsilon$ where $D_{sec} = (1 - d)D$.
- The law describing the damage evolution corresponding a certain strain level ε.
- The damage criterion or flow rule ψ that specifies the elastic domain.

2.2.2 Isotropic Damage Theory

Once the 1D simplification has been described, it is time to extend the damage theory to the general multi-axial states by means of an isotropic damage model with a unique scalar variable.

The isotropic damage models are based on the simplifying assumption that the stiffness degradation is isotropic, i.e., stiffness moduli corresponding to different directions decrease proportionally and independently of direction of loading. Consequently, the damaged constitutive tensor is expressed as

$$\mathbf{D}_{sec} = (1 - d)\mathbf{D} \tag{2.81}$$

where $\mathbf{D}$ is elastic stiffness matrix of the undamaged material and d is the damage parameter. Initially, d is set to zero, representing the virgin undamaged material, and the response is linear-elastic. As the material undergoes the deformation, the initiation and propagation of micro-defects decreases the stiffness, which is represented by the growth of the damage parameter d. For $d = 1$, the stiffness completely disappears. In the present context, the $\mathbf{D}_{sec}$ matrix represents the secant stiffness that relates the total strain to the total stress $\boldsymbol{\sigma}$, according to:

$$\boldsymbol{\sigma} = \mathbf{D}_{sec}\boldsymbol{\varepsilon} = (1 - d)\mathbf{D}\boldsymbol{\varepsilon} \tag{2.82}$$

Furthermore, the Eq. (2.82) can be written as:

$$\boldsymbol{\sigma} = (1 - d)\overline{\boldsymbol{\sigma}} \tag{2.83}$$

Which is the multidimensional generalization of the Eq. (2.79), and where the $\overline{\boldsymbol{\sigma}}$ is the *effective stress tensor* defined as:

$$\overline{\boldsymbol{\sigma}} = \mathbf{D}\boldsymbol{\varepsilon} \tag{2.84}$$

Similar to the uni-axial case, we introduce a loading function ψ specifying the elastic domain and the states at which damage grows. In the damage theory, it is natural to work in the strain space (stress space can be used too) and therefore the loading function is depending on the strain and on an additional parameter κ, describing the evolution of the damage. Physically, κ is a scalar measure of the largest strain level ever reached. The loading function usually has the form:

$$\psi(\boldsymbol{\varepsilon}, \kappa) = \widehat{\varepsilon}(\boldsymbol{\varepsilon}) - \kappa \tag{2.85}$$

where $\widehat{\varepsilon}(\boldsymbol{\varepsilon})$ s the equivalent strain, i.e., the scalar measure of the strain level. Damage can grow only if current state reaches the boundary of elastic domain ($\psi = 0$). This is expressed by the following loading/unloading conditions:

$$\psi \leq 0 \qquad \dot{\kappa} \geq 0 \qquad \dot{\kappa}\psi = 0 \tag{2.86}$$

The important advantage of this explicit formulation is that the stress corresponding to the given strain can be evaluated directly, without the need to solve the non-linear system of equations. For the given strain, the corresponding stress is computed simply by evaluating the current equivalent strain, updating the maximum previously reached equivalent strain value κ and the damage parameter and reducing the effective stress according to $\boldsymbol{\sigma} = (1-d)\overline{\boldsymbol{\sigma}}$.

2.2.3 Non-linearity Associated to Damage

As seen in the linear elastic formulation, the elastic stress-strain relation was used to derive the equilibrium equations from the Principle Virtual Works (2.8). Nonetheless, in the previous section was explained that in order to take into account the lost of stiffness due to damage progression, a different stress-strain relation had to be used:

$$\boldsymbol{\sigma} = \mathbf{D}_{sec}\boldsymbol{\varepsilon} = (1-d)\mathbf{D}\boldsymbol{\varepsilon} \tag{2.87}$$

if we introduce the new stress-strain law (2.87) into the general expression of the PVW (2.8) it is obtained that:

$$\int\int_{A^{(e)}} \mathbf{B}^T(1-d)\boldsymbol{DB}tdA\mathbf{a}^{(e)} - \int\int_{A^{(e)}} \mathbf{B}^T\boldsymbol{D}\boldsymbol{\varepsilon}^0 tdA + \int\int_{A^{(e)}} \mathbf{B}^T\boldsymbol{\sigma}^0 tdA - \int\int_{A^{(e)}} \mathbf{N}^T\mathbf{b}tdA - \oint_{l_{(e)}} \mathbf{N}^T\mathbf{t}tda = \mathbf{q}^{(e)} \tag{2.88}$$

where d is the damage parameter.

The previous expression can be rewritten as:

$$\mathbf{K}^{(e)}(d)\mathbf{a}^{(e)} - \mathbf{f}^{(e)} = \mathbf{q}^{(e)} \tag{2.89}$$

where

$$\mathbf{K}^{(e)}(d) = \int\int_{A^{(e)}} \mathbf{B}^T(1-d)\boldsymbol{DB}tdA \tag{2.90}$$

is the secant or damaged stiffness matrix of the element. Like stated before, by assembling the contributions of the different elements of the mesh one can obtain the global matrix equation:

$$\mathbf{K}(d)\mathbf{a} = \mathbf{f} \tag{2.91}$$

where $\mathbf{K}(d)$ is the global secant matrix. Additionally, it is obvious that the damage parameter d is directly dependent on the displacements, i.e. $d = f(\mathbf{a})$. Applying the previous consideration, the expression (2.91) results:

$$\mathbf{K}(\mathbf{a})\mathbf{a} = \mathbf{f} \tag{2.92}$$

which is, indeed, a non-linear system of equations. Thereby, the inclusion of damage mechanics in the classical elasticity theory introduces a non-linearity that must be taken into account when solving this kind of problems. In the next section, a few solving procedures of non-linear system of equations are presented.

2.2.4 Solution of the Non-linear Equations System

In non-linear problems existence and uniqueness of the solution is not guaranteed. Neither it is possible to estimate the computational cost of finding one or more solutions. This means that, in many cases, the correct solution is path dependent and so it depends on the path followed to reach a given equilibrium state. In this regard, in many cases it is advisable to follow the physics of the problem and consider the solution, not only as the response to a given action, but as a full historical sequence of the successive states of equilibrium that go from the reference state to another one.

Apart from the stated above, it is interesting to follow the full history of a non-linear process because it gives more information on the mechanical behaviour of the system (engineering reason); and it also helps tracing the equilibrium path near critical points and facilitates convergence (mathematical reason).

Thereby, the method for solving non-linear solid mechanic problems consists on following the equilibrium path by using incrementation or continuity strategies. Assuming the action and the response is known at a given equilibrium state, a new equilibrium state is sought, located on the same branch of equilibrium path and a certain distance from the previous one.

A brief summary of some solution techniques of the linearized system of equations is presented in this section.

The solution of the following system of non-linear equilibrium equations,

$${}^{i}\Delta\mathbf{f}^{n+1} = -\left({}^{i}\mathbf{J}^{n+1}\right)\left({}^{i+1}\Delta\mathbf{u}^{n+1}\right) \tag{2.93}$$

can be carried out basically by using two different techniques:

- A linearization based on either the standard or modified *Newton-Raphson* techniques.
- *Quasi-Newton* approximation techniques for the Jacobian matrix.

where ${}^{i}\Delta\mathbf{f}^{n+1}$ represents the prescribed force increment , ${}^{i}\mathbf{J}^{n+1}$ the Jacobian operator (which coincides with the tangent stiffness matrix $\mathbf{K}_{tan}$ in static problems) and ${}^{i+1}\Delta\mathbf{u}^{n+1}$ the displacement increment in the $n+1$ load step and i iteration.

Both techniques are mainly different in the way the residual is expanded in the surrounding of the previous solution and in the way to calculate the Jacobian operator.

2.2.4.1 The Newton-Raphson method

This is the fastest convergence method to solve non-linear equations systems using the linearization technique. This technique assumes that the solution is within the *"attractive zone"* , in other words, the solution is convergent in the surrounding of it. In this case, the convergence ratio is quadratic. In this iterative method, it is assumed that the equilibrium equation has the general form,

$$\Delta\mathbf{f} = \mathbf{f}^{int} - \mathbf{f}^{ext} = 0 \tag{2.94}$$

It can also be written through a Taylor approximation series truncated at second term,

$$\begin{aligned} {}^{i+1}\Delta\mathbf{f}^{n+1} \cong \left({}^{i}\Delta\mathbf{f}^{n+1}\right) + {}^{i}\left(\frac{\partial\Delta\mathbf{f}}{\partial\mathbf{u}}\right)^{n+1}\left({}^{i+1}\Delta\mathbf{u}^{n+1}\right) = \\ = \left({}^{i}\Delta\mathbf{f}^{n+1}\right) + \left({}^{i}\mathbf{J}^{n+1}\right)\left({}^{i+1}\Delta\mathbf{u}^{n+1}\right) = 0 \end{aligned} \tag{2.95}$$

In this equation i represents the iteration counter and n is the current load step. Its solution comes from the inversion of the Jacobian operator ${}^{i}\mathbf{J}^{n+1}$. This is:

$${}^{i+1}\Delta\mathbf{u}^{n+1} = -\left({}^{i}\mathbf{J}^{n+1}\right)^{-1}\left({}^{i}\Delta\mathbf{f}^{n+1}\right) \tag{2.96}$$

Thus, the displacement at the end of the linearized process (or when converged), will be

$${}^{i+1}\mathbf{u}^{n+1} = {}^{i}\mathbf{u}^{n+1} + {}^{i+1}\Delta\mathbf{u}^{n+1} \tag{2.97}$$

As stated before, if the problem is static and conservative loads, the Jacobian is equal to the tangent stiffness matrix so it can be obtained:

$${}^{i+1}\mathbf{u}^{n+1} = {}^{i}\mathbf{u}^{n+1} - \mathbf{K}_{tan}\left({}^{i}\mathbf{u}^{n+1}\right)^{-1}\left({}^{i}\Delta\mathbf{f}^{n+1}\right) \tag{2.98}$$

Finally, at the end of each iteration, it is mandatory to check the convergence criterion with one of the following criteria, displacements and residual criterion, respectively.

$$\frac{\|{}^{i+1}\mathbf{u}^{n+1} - {}^{i}\mathbf{u}^{n+1}\|}{\|{}^{i+1}\mathbf{u}^{n+1}\|} \leqslant tol_u \qquad \frac{\|{}^{i}\Delta\mathbf{f}^{n+1}\|}{\|{}^{i}\Delta\mathbf{f}^{0}\|} \leqslant tol_f \tag{2.99}$$

Despite the fast convergence of this method, some drawbacks can be observed such as:

- It always needs a tangent Jacobian operator, which is not easy to obtain in all cases.
- The convergence velocity is very low when the solution is far away.
- In some cases, the problem needs the solution of Eq. (2.98) for antisymmetric Jacobian operators. This turns difficult its inversion.
- The method usually finds local minimum which are very hard to leave afterwards. Then, other auxiliary techniques are required, such as displacement-control methods (arc-length).

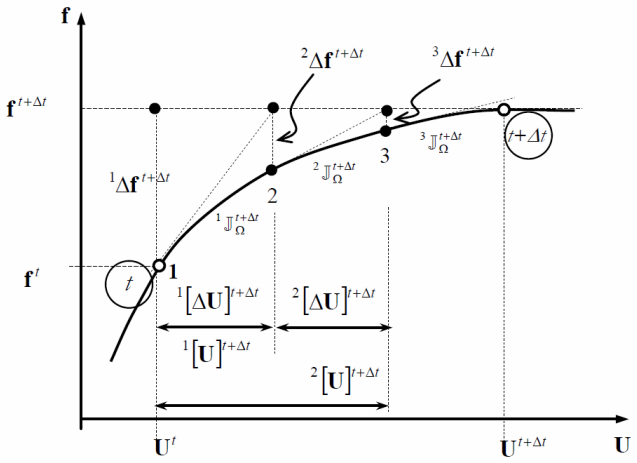

Figure 2.15: Newton-Raphson method [30]

2.2.4.2 The modified Newton-Raphson method

This method solves Eq. (2.96) with the Jacobian operator defined in several forms:

- Initial stiffness method (Fig. 2.16). This numerical technique forces the Jacobian operator to be constant from the beginning to the end of the process.
- Updating time increment method (Fig. 2.17). The Jacobian operator is updated each time the load increases; in other words, while the load is constant there will be no changes in the Jacobian operator.

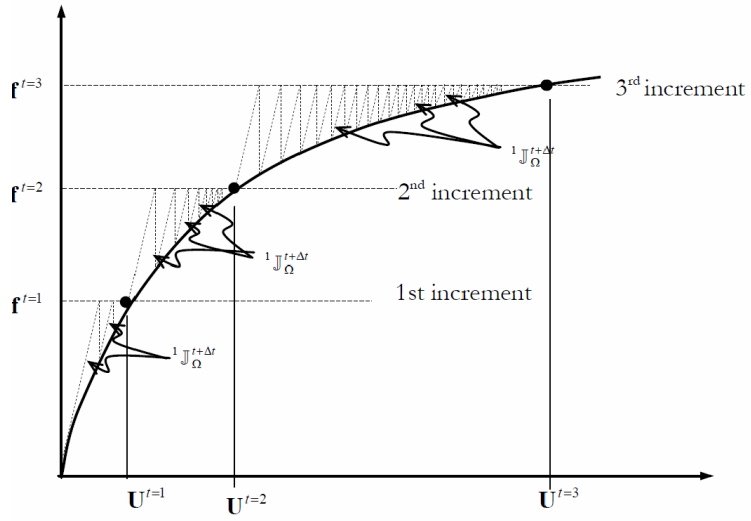

Figure 2.16: Initial stiffness Newton-Raphson method [30]

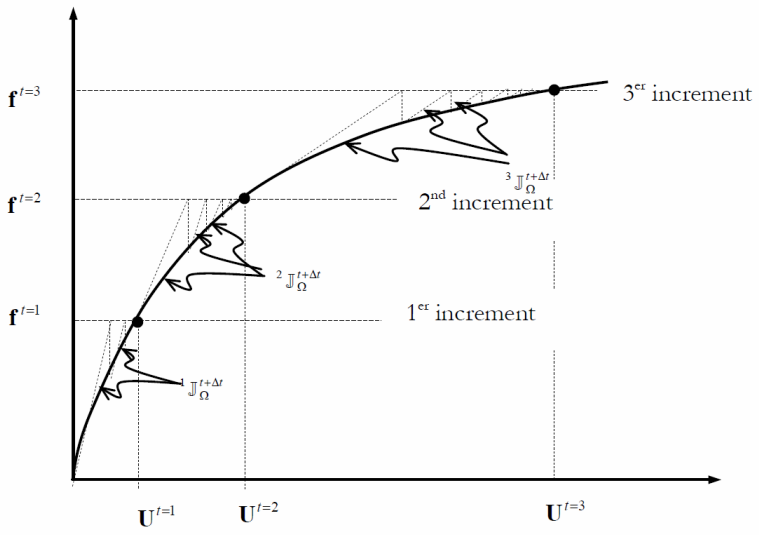

Figure 2.17: Updated Newton-Raphson method at each load increment [30]

The essence of the technique in any of the *"modified Newton"* methods, which is the convergence of speed, is missed and therefore these methods are only used in very particular cases. An example of such cases is when the Jacobian operator has no definition, or when this operator is ill-conditioned. In these cases a decreased convergence speed is generally accepted to obtain at least one solution to the problem.

2.2.5 General Yield Criteria

As seen before, any damage model has to include a function that identifies whether the material is in elastic or plastic regime in order to compute a certain level of degradation. These functions (previously called ψ) are usually known as *yield criterion*.

brief, almost enumerative, description of the yield or plastic discontinuity criteria is presented. The objective of this presentation is to highlight the most significant features of each of them.

A great number of criteria about yield and plastic discontinuity have been formulated during the last years to better represent the plastic behaviour of ideal solids. There are other better suited criteria for the representation of the behaviour of metal and other materials that work better for geomaterials. In general, the formulation and/or use of these criteria require considering the following basic behaviour characteristics:

- **Metallic materials** have traction and compression strength of the same magnitude. The hydrostatic pressure, first invariant stress tensor I_1 , has very little influence on the determination of the plastic yield state.
- **Frictional materials** of the stony concrete type, soils, ceramics, etc., have less strength to traction than to compression. The hydrostatic pressure $p = I_1/3$ has more influence on the plastic yield condition for low and moderate stresses than on high hydrostatic stresses. The solid suffers unrecoverable volume changes showing dilatancy phenomena.

From this brief description the need to formulate different yield and plastic potential criteria to consider the requirements for each type of materials becomes obvious.

2.2.5.1 The Rankine criterion of maximum traction stress

This criterion was formulated by Rankine in 1876 and is based on one single parameter, the maximum uni-axial tension strength σ_T^{max}. Additionally, it is influenced by the first invariant of the stress tensor I_1 and by the second and third invariants of the deviatoric stress tensor J_2 , J_3 , respectively. This criterion helps to set in the limits in a simple way where the fracturing process starts in a point of a solid. This hypothesis leads to the assumption that fractures occur when the maximum main stress reaches the value of the uni-axial tension strength σ_T^{max}.

The mathematical forms to to express this criterion are the following:

- As a function of the principal stresses:

$$\mathcal{F}(\boldsymbol{\sigma}, \sigma_T^{max}) = max(\sigma_I) - \sigma_T^{max} = 0 \tag{2.100}$$

-As a function of the invariants of the stress tensor and its deviatoric stress tensors:

$$\mathcal{F}(I_1, J_2, \theta, \sigma_T^{max}) = 2\sqrt{3J_2}cos(\theta + \pi/6) + I_1 - 3\sigma_T^{max} = 0 \tag{2.101}$$

where θ is the Lode's similarity angle $\theta = asin\left(\dfrac{3\sqrt{3}J_3}{2J_2^{3/2}}\right)$.

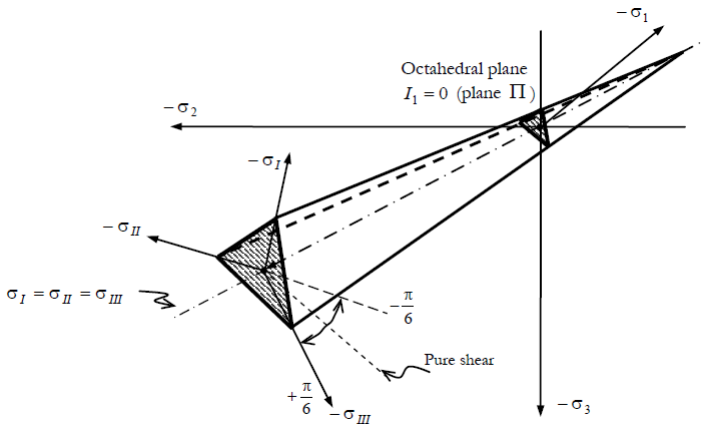

Figure 2.18: Rankine yield surface in the principal stress space [30]

2.2.5.2 The Tresca criterion of maximum shear stress

This criterion was formulated by Tresca in 1864. Similarly to Rankine criterion, it also depends on one single parameter which is the maximum tangent strength τ^{max}. Moreover, it considers the second and third invariants of the deviatoric stress tensor J_2 , J_3 , respectively, neglecting the influence of the first invariant of the stress tensor I_1.

The various mathematical forms to express this criterion are the following:

- As a function of the principal stresses:

$$\mathcal{F}(\boldsymbol{\sigma}, \tau_T^{max}) = max(0.5(\sigma_i - \sigma_j) - \tau^{max} = 0 \tag{2.102}$$

-As a function of the invariants of the stress tensor and its deviatoric stress tensors:

$$\mathcal{F}(J_2, \theta, \tau^{max}) = \sqrt{\frac{J_2}{3}} cos(\theta) - \tau^{max} = 0 \tag{2.103}$$

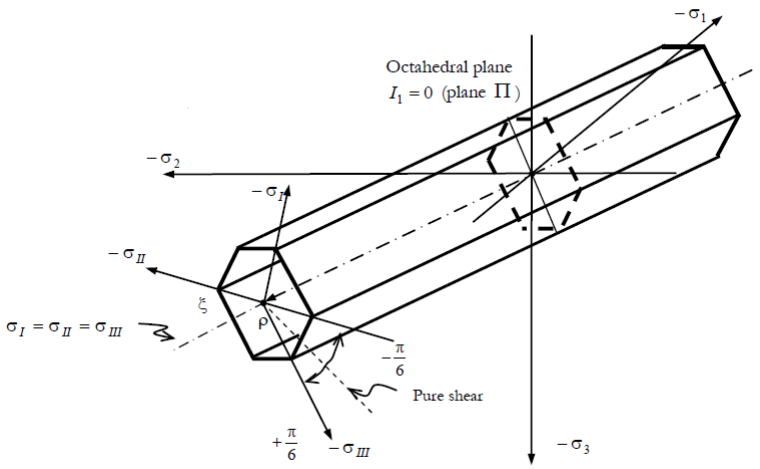

Figure 2.19: Tresca yield surface in the main stress space [30]

2.2.5.3 The Von Mises criterion of octahedral shear stress

This criterion was formulated by Von Mises in 1913, and like the two former, depends only on one single parameter, the maximum octahedral shear strength τ_{oct}^{max}. Moreover, it only considers the second invariant of the stress deviatoric tensor J_2, neglecting hence the influence of the first invariant of the stress tensor I_1 and the third invariant of the stress deviatoric tensor J_3. The different mathematical forms to express this criterion are the following:

-As a function of the main stresses:

$$\mathcal{F}(\boldsymbol{\sigma}, \tau_{oct}^{max}) = \frac{1}{6}\left[(\sigma_1 - \sigma_2)^2 + (\sigma_2 - \sigma_3)^2 + (\sigma_3 - \sigma_1)^2\right] - (\tau_{oct}^{max})^2 = 0 \quad (2.104)$$

-As a function of the invariants of the stress tensor and its deviatoric stress tensors:

$$\mathcal{F}(J_2, \tau_{oct}^{max}) = J_2 - (\tau_{oct}^{max})^2 = 0 \quad (2.105)$$

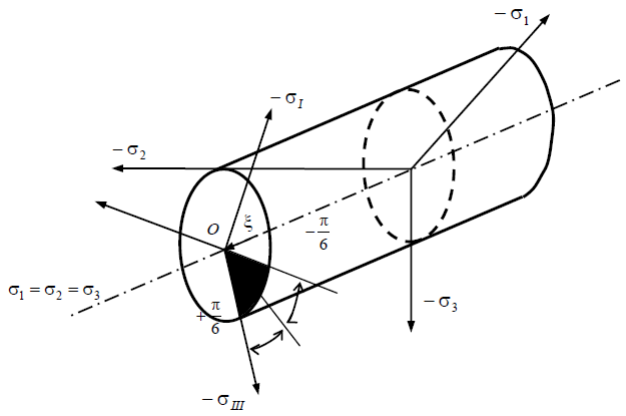

Figure 2.20: Von Mises yield surface in the principal stress space [30]

2.2.5.4 The Mohr-Coulomb criterion of octahedral shear stress

This criterion was first formulated by Coulomb in 1773 and later developed more thoroughly by Mohr in 1882. It is based on two parameters: the cohesion c and the internal friction angle ϕ among particles. It includes the first invariant of the stress tensor in its mathematical expression I_1 and the second and third invariants of the deviatoric stress tensor J_2 , J_3 respectively.

The different mathematical forms to express this criterion are the following:

-As a function of the main stresses:

$$\mathcal{F}(\boldsymbol{\sigma}, \phi, c) = \left[\frac{\sigma_1 - \sigma_3}{2}\right] + \left[\frac{\sigma_1 + \sigma_3}{2}\right] sin(\phi) - cos(\phi)c = 0 \tag{2.106}$$

where σ_1 and σ_3 represent the major and minor principal stresses respectively. Accordingly, it can be deduced that the Mohr-Coulomb criterion neglects the effect of the intermediate principal stress σ_2 , which is a great limitation.

-As a function of the invariants of the stress tensor and its deviatoric stress tensors:

$$\mathcal{F}(I_1, J_2, \theta, c, \phi) = \frac{I_1}{3} sin(\phi) + \sqrt{J_2}\left(cos(\theta) - \frac{sin(\theta)sin(\phi)}{\sqrt{3}}\right) - \sqrt{6}cos(\phi)c = 0 \tag{2.107}$$

These functions describe in the principal stress space a deformed hexagonal-based pyramid, whose axis coincides with the isostatic pressure axis $\sigma_1 = \sigma_2 = \sigma_3$.

From the functions describing the Mohr-Coulomb yield criterion, it is clear that their main characteristic is their capacity to distinguish the traction behaviour from the compression behaviour. Hence, according to this criterion the strength relation of tension and compression satisfies the following expression:

$$R_{Mohr} = \frac{\sigma_c}{\sigma_c} = tan^2\left(\frac{\pi}{4} + \frac{\phi}{2}\right) \tag{2.108}$$

This definition has an important limitation for the criterion adaptation into a particular material as this co-relation does not normally take place in real materials.

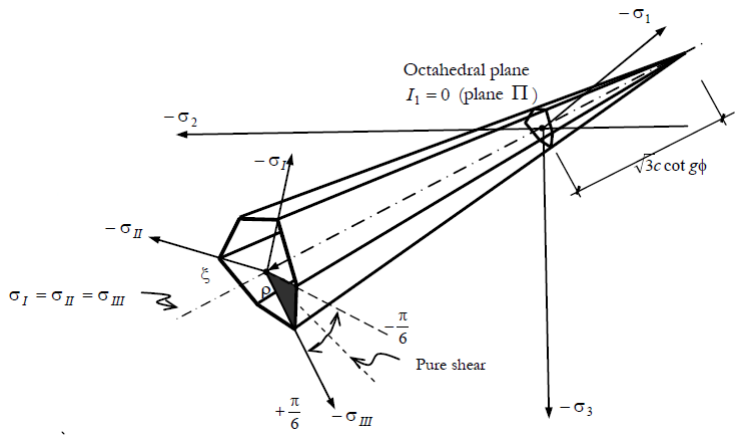

Figure 2.21: Mohr-Coulomb yield surface in the principal stress space [30]

2.2.5.5 The Drucker-Prager criterion

This criterion formulated by Drucker and Prager in 1952 is considered as a smoothed approximation to the Mohr-Coulomb criterion. However, the mathematical formulation arises from a generalization of the Von Mises criterion to include the influence of pressure, through the first invariant of the stress tensor I_1 and the internal friction angle ϕ.

The various forms of mathematically expressing this criterion are the following:

-As a function of the invariants of the stress tensor and its deviatoric tensor:

$$\mathcal{F}(I_1, J_2, c, \phi) = \alpha(\phi) I_1 + \sqrt{J_2} - \mathcal{K} = 0 \tag{2.109}$$

being $\alpha = 2sin(\phi)/(3\sqrt{3} + \sqrt{3}sin(\phi))$ and $\mathcal{K} = 6cos(\phi)c/(3\sqrt{3} + \sqrt{3}sin(\phi))$ if we describe a cone inscribed in Mohr-Coulomb's pyramid. In case the cone confines Mohr-Coulomb's pyramid, the traction and compression meridians of both surfaces coincide and the following functions are obtained from them $\alpha = 2sin(\phi)/(3\sqrt{3} - \sqrt{3}sin(\phi))$ and $\mathcal{K} = 6cos(\phi)c/(3\sqrt{3} - \sqrt{3}sin(\phi))$. Both particular cases describe two completely different behaviours.

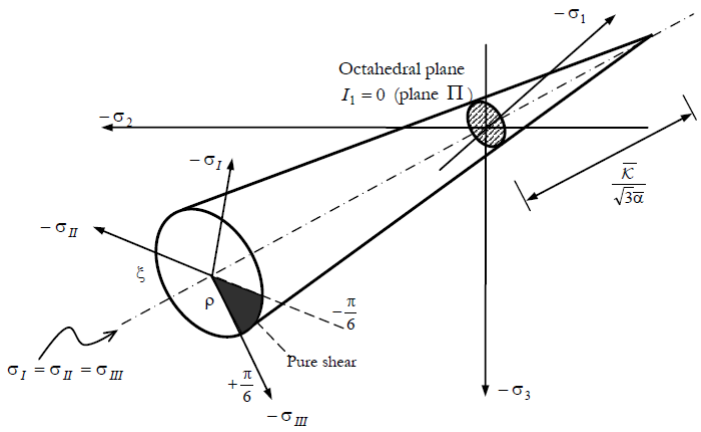

Figure 2.22: Drucker-Prager yield surface in the principal stress space [30]

2.2.6 Damage Evolution Laws

As stated for the uni-axial case, one of the basic components of a damage model is the law governing the evolution of the damage variable. There are various damage governing laws that can be effectively used to model damage growth in geo-materials, and in the following lines some of the most used models are presented.

2.2.6.1 Exponential softening

The scalar function g defining the evolution of the damage threshold must be monotonous and with a value ranging from 0 to 1. This scalar function can be described as [29]:

$$g(f(\boldsymbol{\sigma}_0)) = 1 - \frac{f^0(\boldsymbol{\sigma}_0)}{f(\boldsymbol{\sigma}_0)} e^{A\left(1 - \frac{f(\boldsymbol{\sigma}_0)}{f^0(\boldsymbol{\sigma}_0)}\right)} \tag{2.110}$$

where A is a parameter that depends on the fracture energy of the material. The value of $f^0(\boldsymbol{\sigma}_0)$ is obtained from the fulfilment of the damage criterion for the first threshold of degradation.

2.2.6.2 Linear softening

For linear softening a new definition of the scalar function g is given for the damage threshold. As in the previous section, this function must be monotone increasing and ranging from 0 to 1. This is:

$$g(f(\boldsymbol{\sigma}_0)) = \frac{1 - \dfrac{f^0(\boldsymbol{\sigma}_0)}{f(\boldsymbol{\sigma}_0)}}{1 + A} \tag{2.111}$$

where A is a parameter that depends on the fracture energy of the material. The initial value of $f^0(\boldsymbol{\sigma}_0)$ is obtained from the damage criterion.

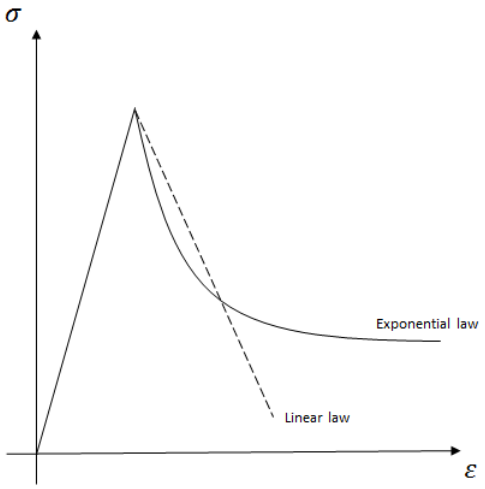

Figure 2.23: Linear and exponential softening laws

Chapter 3

Overview of the Discrete Element Method

Since the FEM-DEM formulation implies the generation of discrete elements inside the finite element mesh, it is necessary to review the principal characteristics of the Discrete Element Method.

Extensive research work on the discrete element method (DEM) has been carried out in the last decades since the first ideas were presented by Cundall and Strack [6]. Much of the research efforts have focused on the development of adequate DEM models for accurately reproducing the correct behaviour of non cohesive and cohesive granular assemblies as well as of solid materials. In recent years the DEM has also been effectively applied to the study of multi-fracture and failure of geo-materials (soils and rocks), concrete, masonry and ceramic materials, among others.

3.1 Introduction to the Discrete Element Method

Within the analysis of solids with the DEM the material is typically represented as a collection of rigid particles (spheres in three dimensions (3D) and discs in two dimensions (2D)) interacting among themselves at the contact interfaces in the normal and tangential directions. Material deformation is assumed to be

concentrated at the contact points. Appropriate contact laws are defined in order to obtain the desired macroscopic material properties. The contact law can be seen as the formulation of the material model of the underlying continuum at the microscopic level. For frictional cohesive material the contact law takes into account the cohesive bonds between rigid particles. Cohesive bonds can be broken, thus allowing to simulate fracture of the material and its propagation.

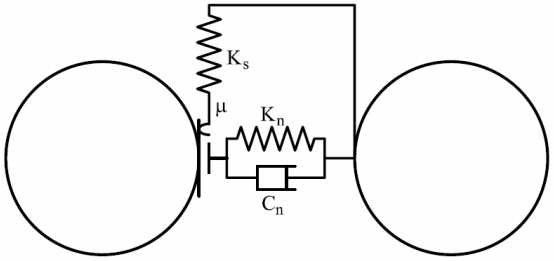

Figure 3.1: Model of the contact interface in the DEM [28]

A challenge in the failure analysis of solid materials, such as cement, shale rock and concrete, with the DEM is the definition of the limit strengths in the normal and shear directions at the contact interfaces, and the characterization of the non linear relationship between forces and displacements at these interfaces beyond the onset of fracture, accounting for frictional effects, damage and plasticity.

3.2 Earliest Formulations DEM

Because this chapter's objective is to introduce the DEM, the earliest and simplest formulations are presented, which are, additionally, the better way to understand the procedures of the DEM. The first formulations of the DEM were based on rigid circular 2D solids with deformable contacts. The general solving scheme is direct, typically formulated by means of a explicit time integration [6]. The solid movement is governed by the external loads and the contact forces acting on a certain particle. The method carry out a loop over all the solids and, for each time step, compute all the forces acting on them. The unbalanced forces (or moments) produce accelerations (translational or rotations) that determines the movement of that solid in the next time step.

The simplest computational procedure for the DEM solves the movement equations on a certain discrete element and then updates the contact forces due to the contact between another particle or the boundary.

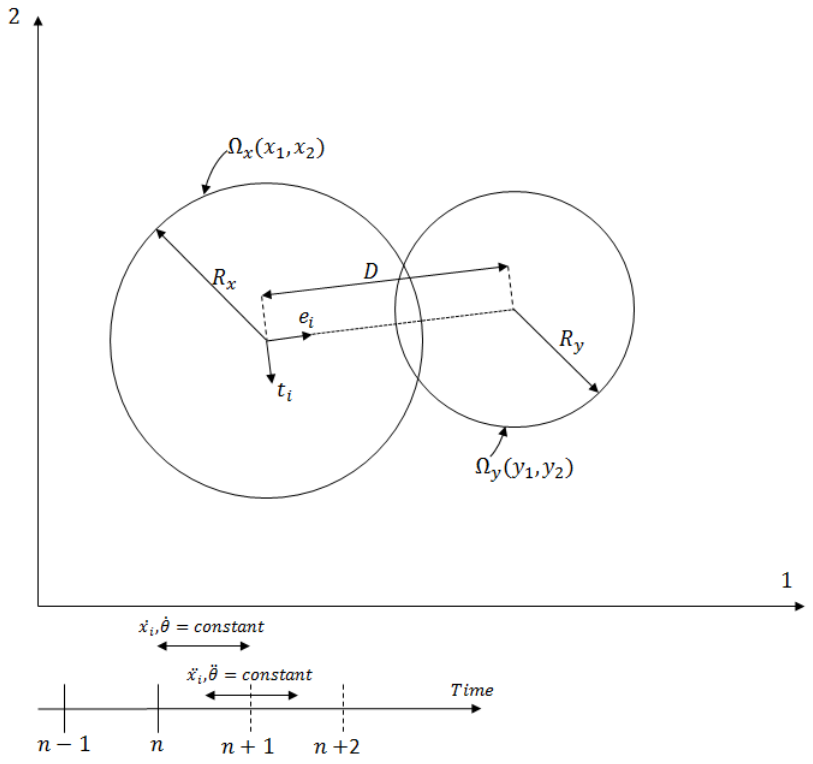

Figure 3.2: Discrete element method scheme

As is shown in the Fig. 3.2, at each time step, the coordinates of the two particles (Ω_x, Ω_y) are known ((x_1, x_2) and (y_1, y_2) respectively). The radius of the particles are the R_x and R_y and the distance between the centers of the particles is D. Additionally, the translational velocity $(\dot{x_i}, \dot{y_i})$ and the angular velocity $(\dot{\theta_i}, \dot{\theta_i})$ of each particle must be known for each i direction. Finally, in the same figure can be identified the unitary vectors (e_i and t_i) that connects the two centers of the particles.

Once the previous variables have been presented, the relative velocities in the i direction can be calculated as:

$$\dot{X}_i = (\dot{x}_i - \dot{y}_i) - (\dot{\theta}_x R_x + \dot{\theta}_y R_y) t_i \tag{3.1}$$

In this context, the relative displacements (Δn and Δs) can be obtained with:

$$\dot{n} = \dot{X}_i e_i \qquad \dot{s} = \dot{X}_i t_i \tag{3.2}$$

$$\Delta n = \dot{n} \Delta t \qquad \Delta s = \dot{s} \Delta t \tag{3.3}$$

so the contact force increments:

$$\Delta F_n = k_n(\Delta n + \beta \dot{n}) \qquad \Delta F_s = k_s(\Delta s + \beta \dot{s}) \tag{3.4}$$

Adding the contact force increments (Eq. (3.4)) to the previous time step (n):

$$F_n = F_n^n + \Delta F_n \qquad F_s = F_s^n + \Delta F_s \tag{3.5}$$

After this process, the sliding between particles must be checked:

$$F_s = min(F_s, C + F_n tan(\phi)) \tag{3.6}$$

and the moments:

$$M_x = \sum F_x R_x \qquad M_y = \sum F_y R_y \tag{3.7}$$

At this point, all the forces acting on the particles are known so the movement equations can be solved. Firstly, the accelerations are obtained solving the following equations:

$$m\ddot{x}_i = \sum F_i \qquad I\ddot{\theta}_i = \sum M_i \tag{3.8}$$

In the same way the velocities are updated

$$\dot{x}_i^{n+1/2} = \dot{x}_i^{n-1/2} + \ddot{x}_i \Delta t \qquad \dot{\theta}_i^{n+1/2} = \dot{\theta}_i^{n-1/2} + \ddot{\theta}_i \Delta t \tag{3.9}$$

and, in the end, the new displacements:

$$x_i^{n+1} = x_i^n + \dot{x}_i^{n+1/2} \Delta t \qquad \theta_i^{n+1} = \theta_i^n + \dot{\theta}_i^{n+1/2} \Delta t \tag{3.10}$$

With this simple and direct algorithm, proposed initially by Cundall and Strack [6], one can obtain, in each time step, the displacements, accelerations and velocities according to an unbalanced system of equations in each particle.

Chapter 4

The FEM-DEM Formulation

In this chapter the FEM-DEM formulation used in the posterior examples is presented. As stated before, the formulation uses the FEM to model a continuum whose fracture is described by means of discrete elements when it appears. The FEM-DEM transition is done without remeshing. This chapter describes the basis of the simple FEM-DEM procedure proposed. The method extends a well defined crack opening methodology termed Element Elimination Technique (EET) [13], [22], [34] that creates discrete elements at the crack lips. Onset of cracking at the mid-point of the element sides is governed by a standard single parameter damage model [5], [3], [8]. This is followed by the removal of the side and the generation of discrete elements at the nodes sharing the side. Some important aspects inherent to the formulation here presented guarantee the good results obtained like a smoothed stress field, mass conservation and the use of a simple algorithm to ensure the post-fracture contact

4.1 From FEM to DEM

The DEM is a very powerful tool when it is used for analysis of granular materials. Its main advantage when applied to a continuous domain is it capability for

predicting random cracking paths, which is useful for reproducing correctly the fracture behaviour of materials such as soils, rocks, ceramics and concrete, among others. Thus, the rationale of the FEM-DEM approach proposed in this work is to apply the DEM methodology for modelling the onset and evolution of a crack to the standard FEM formulation.

In order to eliminate properly a cohesive bond it is necessary to define a failure criterion. It is important to note that cohesive bonds are assumed to be placed at the element sides and not at the integration point within the element. Recalling that the stress field is discontinuous between elements, a smoothing procedure is needed to evaluate the stresses at the element edges and, subsequently, the failure criteria chosen at the edges.

The failure criterion chosen is based on the standard single parameter damage model, typically used for predicting the onset of fracture in concrete and ceramic materials. The damage model is summarized below.

4.1.1 Computation of the Remaining Stiffness for an Element

In this work a standard single parameter damage model is used. The constitutive equation at the element center is therefore simply written as [38]:

$$\boldsymbol{\sigma} = (1 - \tilde{d})\mathbf{D}\boldsymbol{\varepsilon} \tag{4.1}$$

where

$$\tilde{d} = \frac{1}{3}(d_1 + d_2 + d_3) \tag{4.2}$$

is the average damage over the three edges. In this context, the remaining damaged stiffness can be computed with:

$$\mathbf{K}^{(e)} = (1 - \tilde{d})\mathbf{K}_0^{(e)} = \mathbf{K}_0 - \tilde{\mathbf{K}}^{(e)} \tag{4.3}$$

where $\mathbf{K}_0^{(e)}$ is the stiffness matrix of the undamaged material whereas the damaged stiffness matrix is computed as follows:

$$\tilde{\mathbf{K}}^{(e)} = \frac{1}{3}(d_1 + d_2 + d_3)\mathbf{K}_0^{(e)} \tag{4.4}$$

A key issue in this approach derives from analyzing in detail the Eq. (4.4). As is shown in the Fig. 4.1, when the element has two fully damaged edges, according to the Eq. (4.4) the damaged stiffness is one-third of the original one. However, the fact is that a crack has already appeared within the element and, therefore, when two sides of an element are fully damaged the whole element can be considered to

be as fully damaged as well. Consequently, the remaining stiffness for a damaged element must be computed as:

$$\tilde{\mathbf{K}}^{(e)} = \frac{1}{2}(d_i + d_j)\mathbf{K}_0^{(e)} \tag{4.5}$$

where d_i and d_j are the two maximum values of the damage parameters for the three element edges.

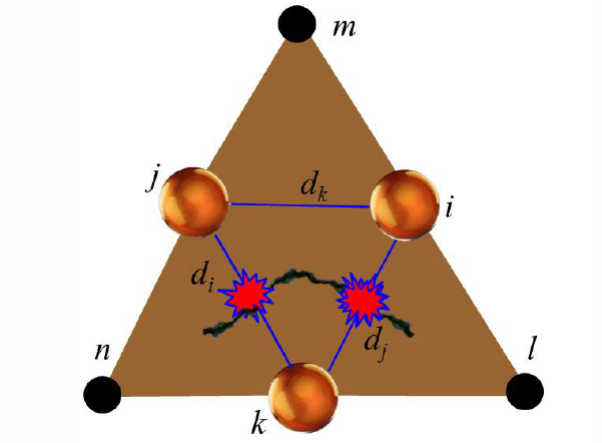

Figure 4.1: Triangular linear element with two edges fully damaged [38]

4.1.2 Damage Evolution Model

In this formulation, the Mohr-Coulomb yield surface is considered. As stated in the section 2.2.5.4, the Mohr-Coulomb criterion is widely used in the simulations of frictional materials such as rocks and concrete, which is one of the objectives of the FEM-DEM formulation presented. In the FEM-DEM formulation, damage is assumed to initiate at the element mid-sides once the stress field satisfies the Mohr-Coulomb criterion. This is schematically shown in Fig. 4.2 for a 2D stress state.

The evolution of the damage variable d at the midpoint of the element sides is defined by the following exponential function (see chapter 2.2.6)

$$d(\sigma) = 1 - \frac{c^{max}}{f(\sigma)} \exp\left(A\left(1 - \frac{f(\sigma)}{c^{max}}\right)\right) \tag{4.6}$$

where $f(\sigma)$ is the equivalent stress state according to a certain yield surface and

c^{max} is obtained from the fulfilment of the damage criterion for the first threshold of degradation. Fig. 4.2 shows an schematic representation of δ, which is the distance between the yield surface and three different stress points S_1, S_2, S_3. Note that for points laying on the yield surface $\delta = 0$ and, hence, $\tilde{\delta} = 1$ and $d(1) = 0$. On the other hand $d(\infty) = 1$, as expected.

In the Eq. (4.6), the A parameter is determined from the energy dissipated in an uni-axial tension test as

$$A = \left(\frac{G_f E}{\hat{l} f_t^2} - \frac{1}{2} \right)^{-1} \tag{4.7}$$

where f_t is the tensile strength, G_f is the specific fracture energy per unit area (taken as a material property) and $\hat{l}$ is the characteristic length of the fractured domain (currently is the edge length). The damage model presented above is extremely simple in comparison with more sophisticated constitutive models for concrete and other frictional materials [5],[17], [31].

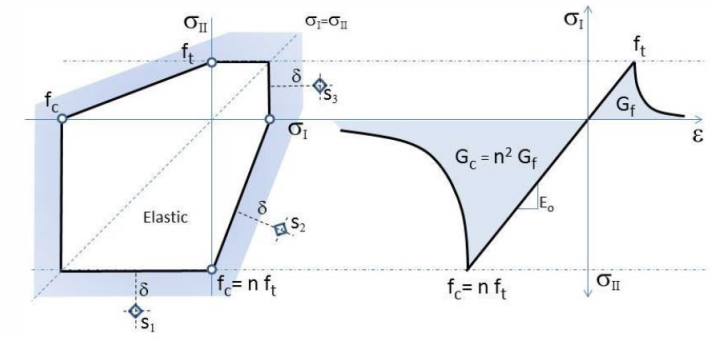

Figure 4.2: Mohr-Coulomb criterion in the 2D principal stress space and the uni-axial stress-strain curve for the damage model [38]

4.1.3 Generation of Discrete Particles

When a cohesive bond is fully removed (*i.e.* the side stiffness is neglected) two discrete elements (or particles) are created at the disconnected nodes. In this case circular discs (for 2D problems) and spheres (for 3D problems) have been used in order to simulate the discrete elements. The mass of each new discrete element corresponds to the nodal mass and its radius will be the maximum one that guarantees the contact between the adjacent discrete elements without creating any overlappings between them. Indeed, this is not the only algorithm that can

be used for generating discrete elements but it has been proved to be a very effective procedure, as the main idea is to avoid that the new discrete elements created generate spurious contact forces [28].

Once an discrete element is created, the forces at the contact interfaces are used to define the interaction of the element with the adjacent ones. These forces are due only to the contact interaction in the normal and tangential directions. At the contact point, the minimum radius of the particles in contact are used to evaluate the contact forces. In this work, a local constitutive model for the normal and tangential forces at the contact interfaces between discrete elements is used. For 2D problems the normal contact force F_n at a contact point between two discs is given by:

$$F_n = E_0 A \varepsilon_n = 2E_0 rt \left(\frac{u_n}{r_i + r_j} \right) \tag{4.8}$$

with $r = min(r_i, r_j)$ and u_n is the normal overlap between the two discrete elements.

The tangential force F_s at the contact point is a function of the relative tangential displacement us between the two particles in contact, and is defined in a regularized way as:

$$F_s = min \left\{ 2rt \left(\frac{u_n}{r_i + r_j} \right) \frac{E_0}{2(1+\nu)}; \mu F_n \right\} \tag{4.9}$$

The extension of the previous equations to the 3D can can be seen in [28], [38]. Some interesting facts are derived from this approach. Since the number of discrete elements generated in an analysis is only a fraction of the number of nodes of the mesh, the searching algorithm for evaluating the contact interactions between discrete elements does not consume much computational resources, as in the case of using discrete elements only. Additionally, the generated particles undergo relatively small displacements (due to the time increments used in the explicit integration scheme chosen here) so the list of possible contact points does not require a constant updating.

4.2 3D FEM-DEM Formulation

As stated in the chapter 2.1.2, the 3D FEM-DEM formulation uses the linear tetrahedra finite element in the calculations. The only relevant difference between the 2D and the 3D formulations is the fracture process of the element. In the 2D space, the triangular element is removed from the mesh when two of the sides are fully damaged. On the other hand, in the 3D geometry, the element is removed when one of the two crack planes (see Fig. 4.3) are developed. The stress smooth-

ing procedure and the damage computation can be completely extrapolated from the 2D theory exposed in the previous paragraph.

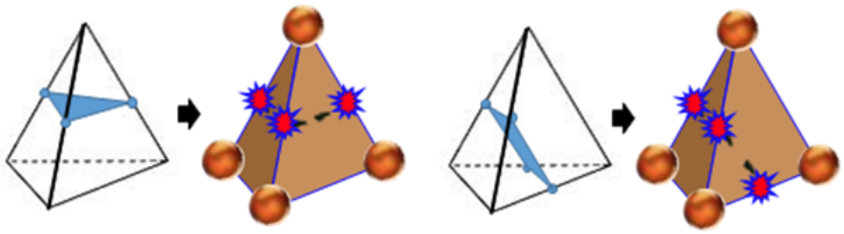

Figure 4.3: Fracture mechanisms of the tetrahedron

4.3 Application Examples

At this point, the necessary concepts on the FEM-DEM formulation have been presented. In this section a compilation of examples are shown. Some of the examples are focused on predicting the behaviour of a certain sample of material subjected to a classical test such as the Brazilian test and the Uni-axial compression test, among others. Additionally, two examples related to mining methods were performed, a tunnel portal and a slope of earth subjected to a sequential blast loading.

It is also important to mention that some of the simulations have been performed in 2D and 3D in order to compare the behaviour of the sample in different dimensions.

4.3.1 Indirect Tensile Test

The Brazilian tensile strength (BTS) test is a very practical and simple experimental procedure to evaluate the tensile strength of brittle materials. In this case a cylinder of 15 cm of diameter (ϕ) and 30 cm of height (H) is analysed. The described sample is loaded diametrically by a press with an imposed velocity of 1 mm/s. The theoretical tensile strength of the material can be computed using the following expression [2]:

$$f_t^{theory} = \frac{2P}{\pi H \phi} \tag{4.10}$$

Parameter	Value
Young's modulus (E)	35000 MPa
Poisson's ratio (ν)	0.2
Compressive strength (σ_c)	30 MPa
Tensile strength (σ_t)	1.50 MPa
Fracture energy (G_f)	75 J/m^2

Table 4.1: Material properties used in the 2D simulations

being P the total applied load.

4.3.1.1 2D Simulation

In this section, the results obtained for the BTS test in 2D are shown. The model can be found in the Fig. 4.4.The previous model consist on a circle with 7.50 cm of radius and a 30 cm of height, the loading surface has width of 1 cm . The properties of the material used in these calculations are described in the table 4.1.

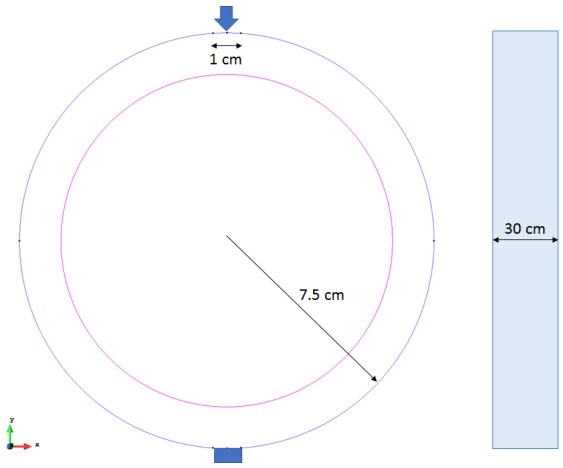

Figure 4.4: Brazilian tensile test sample. Geometry and boundary conditions for the analysis

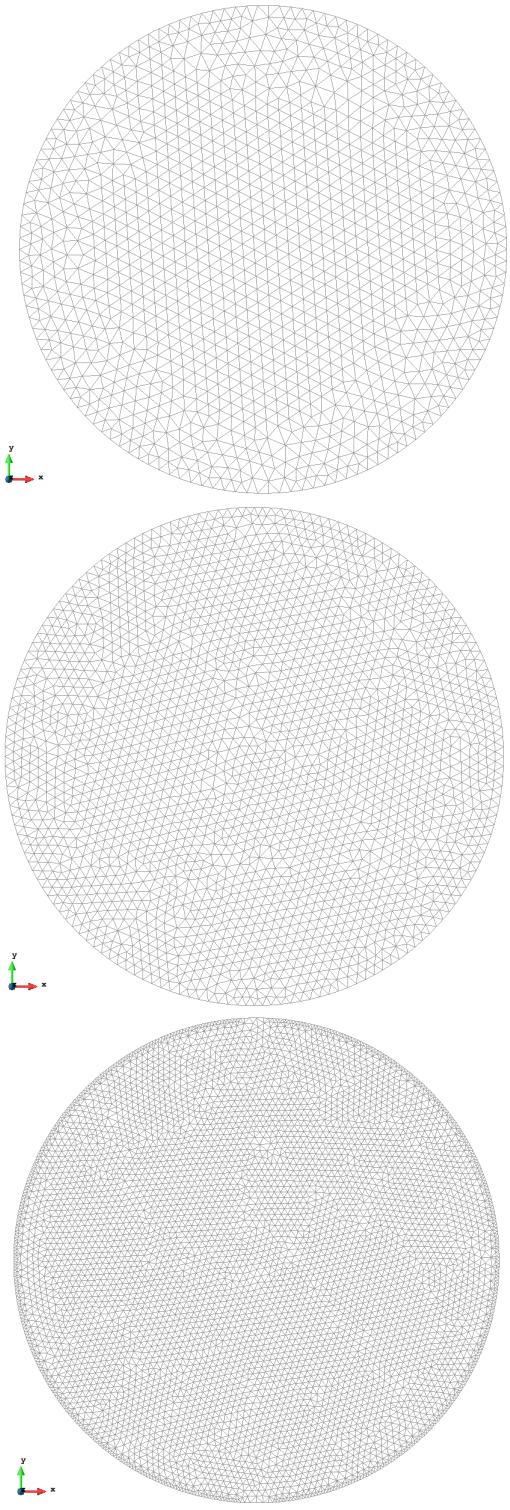

Figure 4.5: Finite element meshes used in the calculations with 2408, 4450 and 10922 elements, respectively

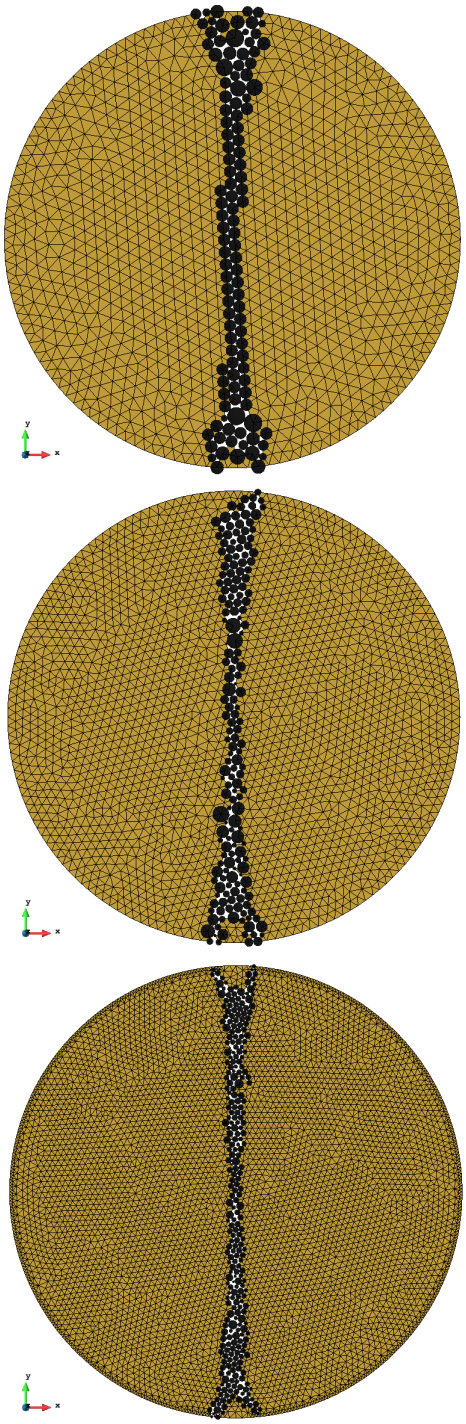

Figure 4.6: Damaged geometry of the sample for each finite element mesh

Fig. 4.6 shows that the crack and the discrete elements generated when the sample is fully damaged is similar for the three meshes and coherent with the theoretical case [1]. Additionally, the numerical values for the tensile strength obtained using the Eq. 4.10 were 1.64 MPa, 1.63 MPa and 1.62 MPa with the coarse, intermediate and fine mesh, respectively.This means that the error is less than a 10% with respect to the analytical solution. The Fig. 4.7 shows the evolution of the vertical applied load versus the vertical displacement at the top of the sample.

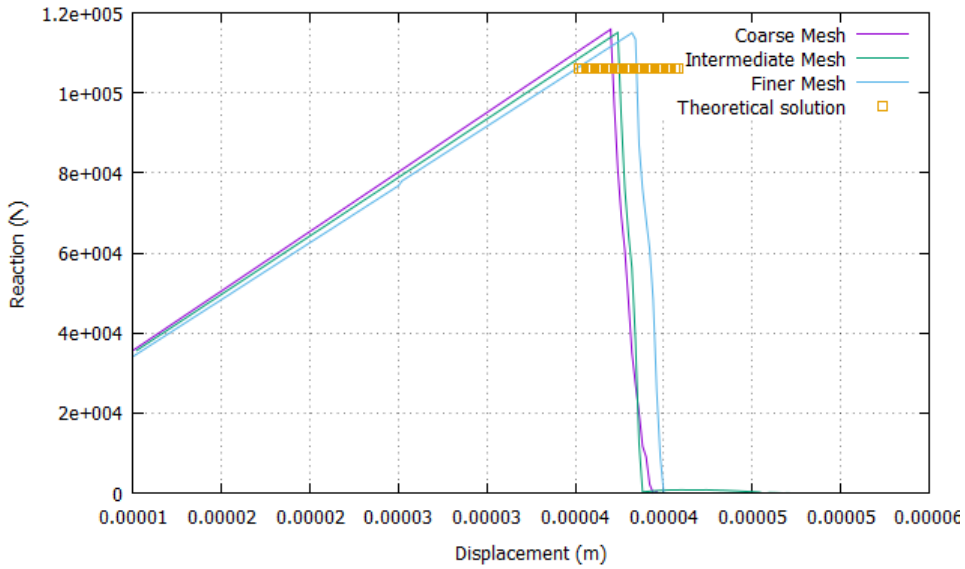

Figure 4.7: Force-displacement relationship for the three meshes used

4.3.1.2 3D Simulation

The same example with identical geometry was solved in 3D using an extension of the FEM-DEM technique presented in this thesis. Analogously, this simulation has been conducted with three different meshes to ensure a well performance of the code. The three used meshes can be found in the Fig. 4.8. The material properties assumed in the 3D simulations are shown in the table 4.2.

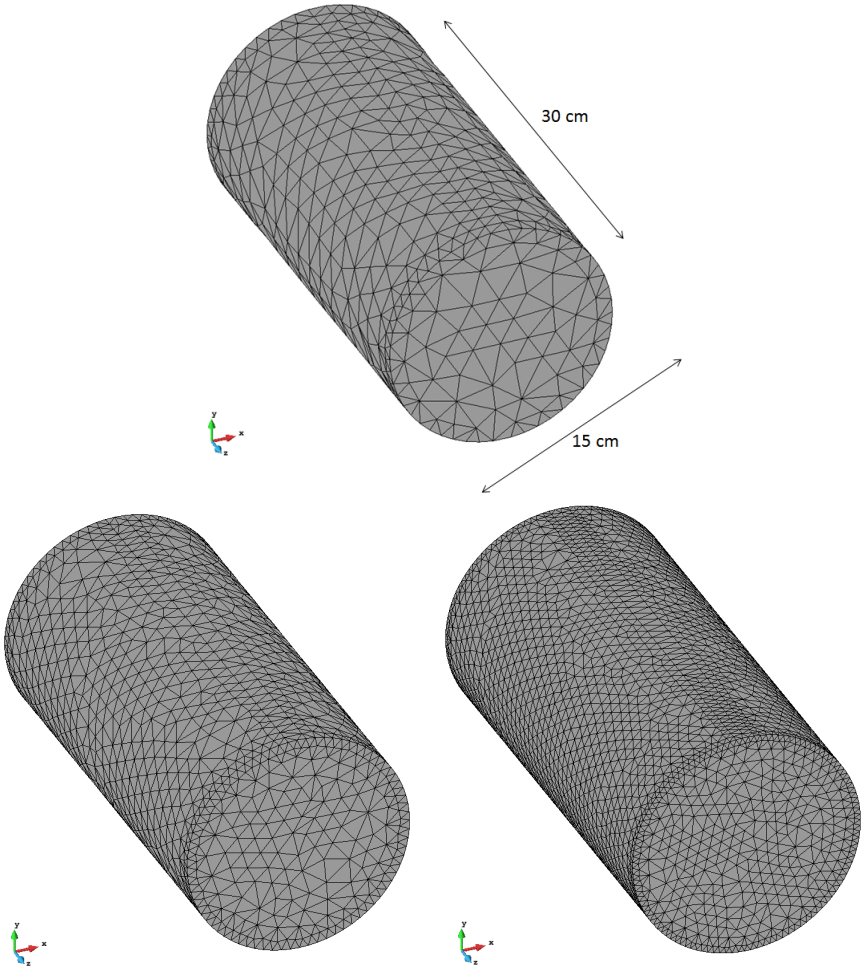

Figure 4.8: Finite element meshes used in the 3D computations containing 9018, 32042 and 107132 linear tetrahedral elements, respectively

Parameter	Value
Young's modulus (E)	35000 MPa
Poisson's ratio (ν)	0.2
Compressive strength (σ_c)	30 MPa
Tensile strength (σ_t)	1.50 MPa
Fracture energy (G_f)	75 J/m^2

Table 4.2: Material properties used in the 3D simulations

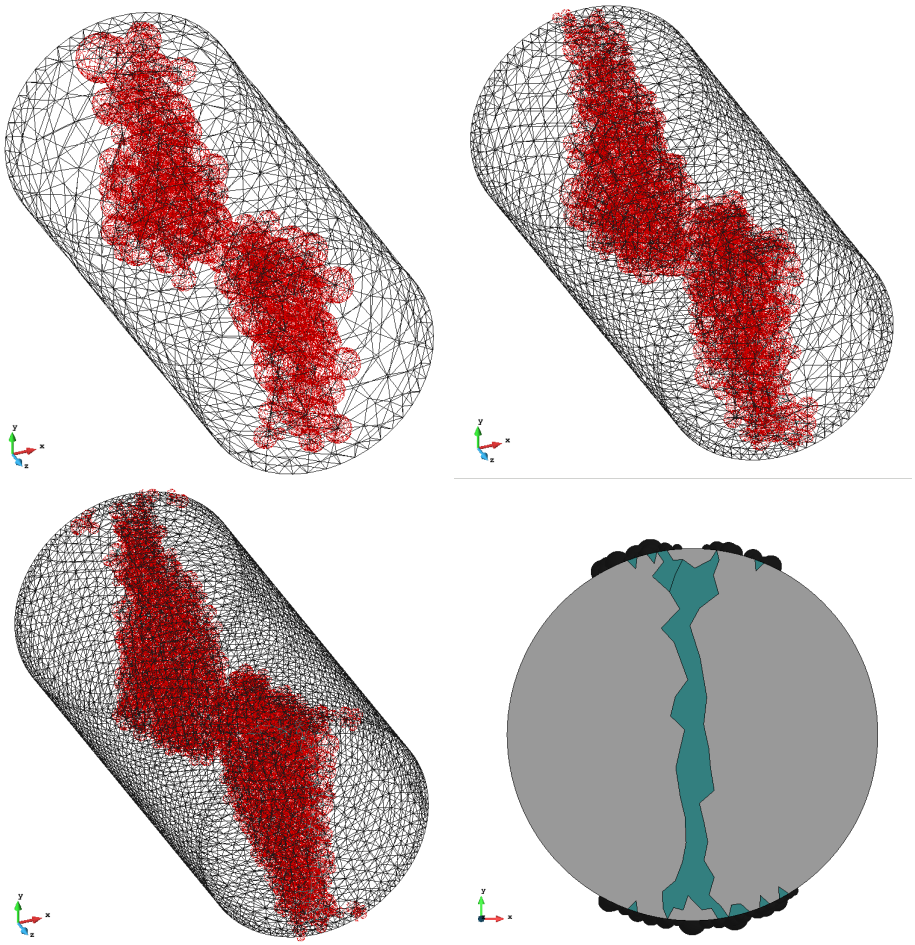

Figure 4.9: Damaged zone and discrete elements generated for the three meshes

The results of the crack pattern and the discrete elements generated for each mesh are depicted in Fig. 4.9. As stated in the 2D case, the crack path is similar in the three cases and does not depend on the mesh refinement. The numerical results for the load-displacement curve are presented in Fig. 4.10. As expected, the coarse mesh is more rigid whereas the finer mesh behaves more flexibly. In this case the simulated tensile strength is 1.68 MPa, 1.64 MPa and 1.56 MPa for the coarse, intermediate and the fine mesh, respectively. This means that the error committed is less than the 10% in comparisson with the analytical solution. In the Fig. 4.11 one can see the high analogy of the damaged path between the simulated a the real test.

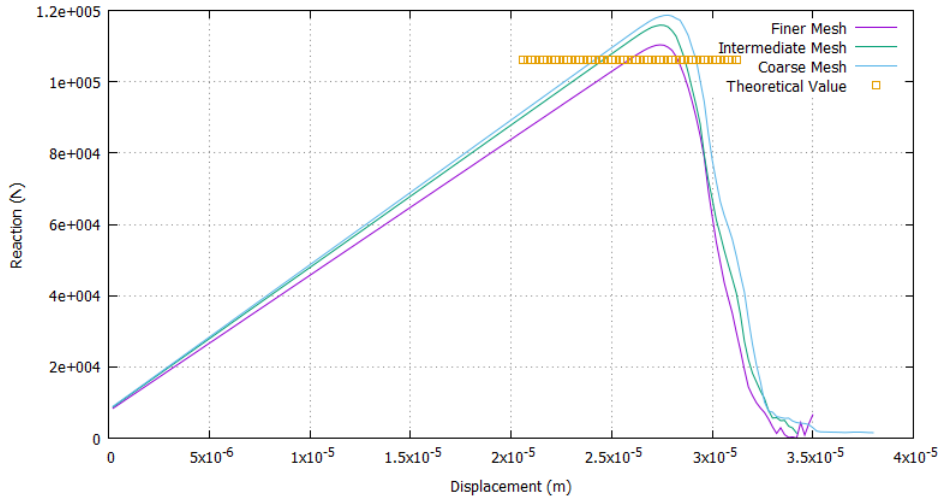

Figure 4.10: Force-Displacement evolution for the three 3D meshes

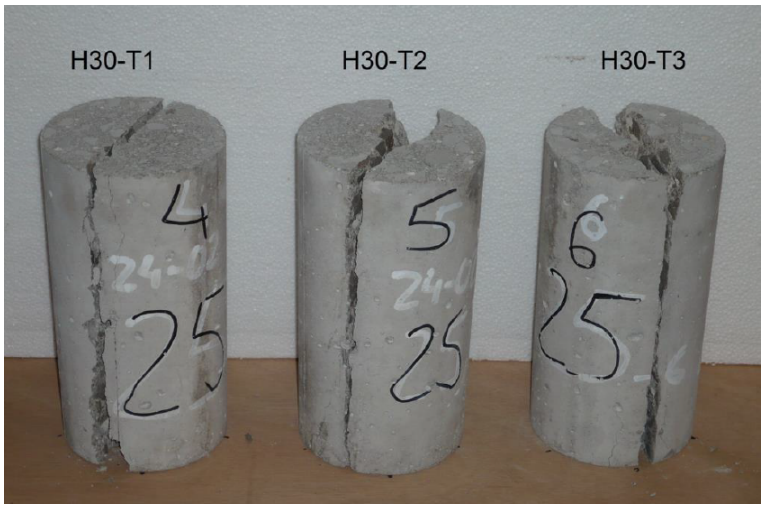

Figure 4.11: Damaged geometry of samples tested in the laboratory [18]

4.3.2 Uni-axial Compression Test

The uni-axial compression (UC) tests provide a simple and effective way to characterize a material's response to loading. By subjecting a sample to a controlled compressive displacement along a single axis, the change in dimensions and resulting load can be recorded to calculate a stress-strain profile. From the obtained curve, elastic and plastic material properties can then be determined. In this context, an standarized concrete specimen whose geometry is defined in the Fig. 4.12 is analysed. The two ends of the specimen are fixed except the vertical loading direction in which the imposed displacement is applied (see Fig.4.12).The material properties of the material are illustrated in the table 4.3. The results of the simulations are shown in the Fig. 4.14. The crack path is similar in both cases and develops as expected [1]. In the Fig. 4.15, one can see that the elastic branch is common in both cases and, in the long term, the finest mesh reaches a highest value of reaction.

Knowing that the top surface of the sample has an area equal to $S = 0.0176m^2$, the maximum stress level in compression of the simulation reaches 29.83 MPa and 29.95 MPa for the coarse and fine mesh, respectively. This demonstrates the high accuracy of the code since the theoretical value is, as described in the table 4.3, 30 MPa. In the Fig. 4.16 one can observe that the crack path in this kind of test is difficult to predict due to the fast failure of the UC test. This fact is reflected in the FEM-DEM simulation because with two different meshes the code obtains two similar crack paths but in different positions of the sample.

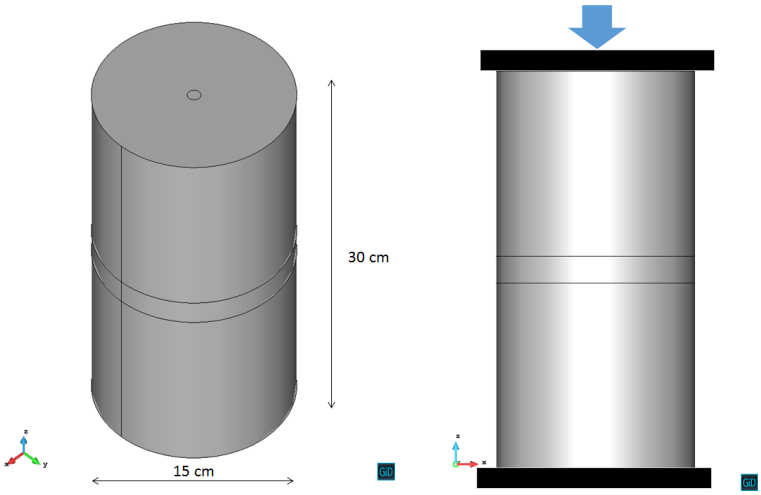

Figure 4.12: Uni-axial compression sample geometry and boundary conditions

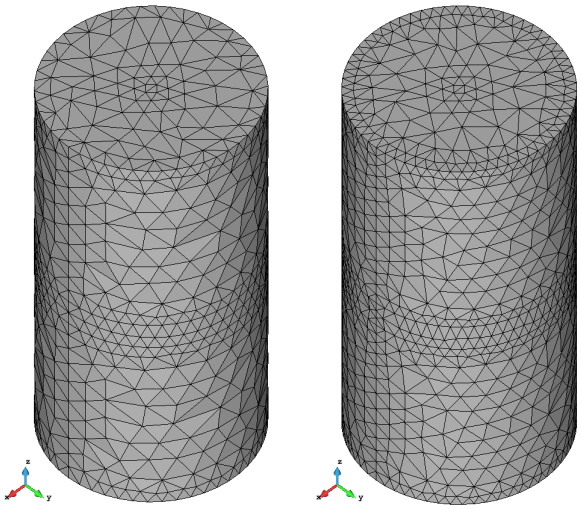

Figure 4.13: Finite element meshes used in the UC tests with 11781 and 21611 elements, respectively

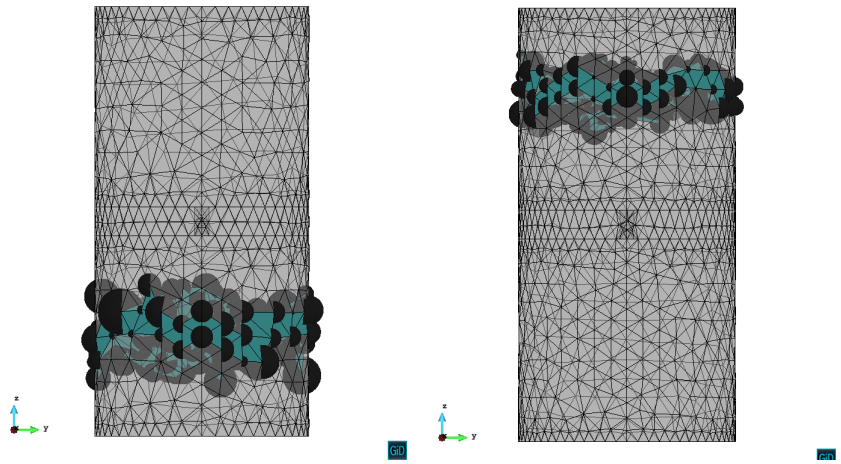

Figure 4.14: Damaged geometry and the discrete elements generated

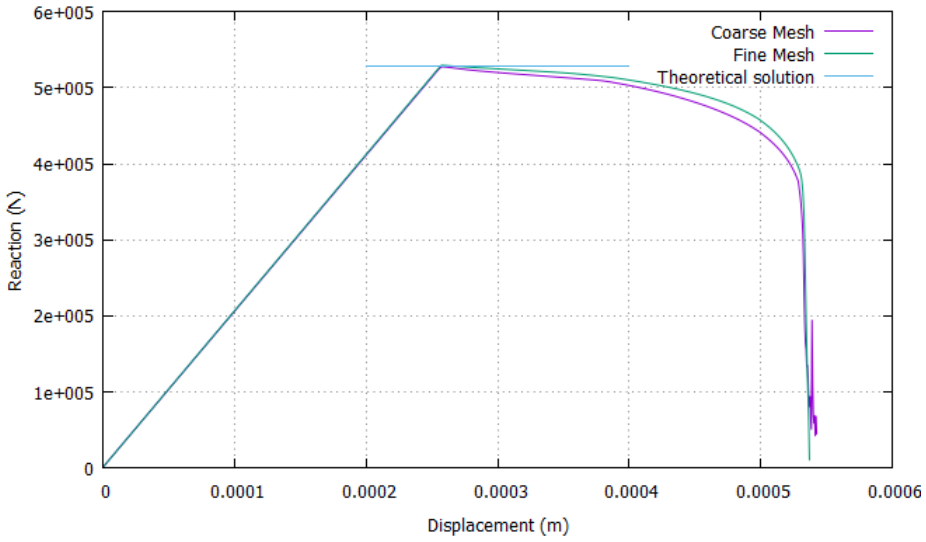

Figure 4.15: Force-Displacement evolution in the UC test for the two meshes

Parameter	Value
Young's modulus (E)	35000 MPa
Poisson's ratio (ν)	0.22
Compressive strength (σ_c)	30 MPa
Tensile strength (σ_t)	3 MPa
Fracture energy (G_f)	75 J/m^2

Table 4.3: Material properties used in the UC test

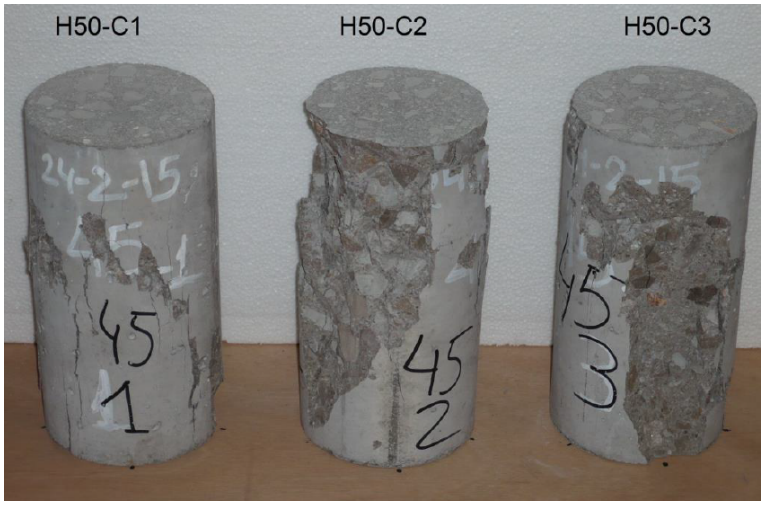

Figure 4.16: Damaged concrete samples analysed in the laboratory [18]

4.3.3 Shear Test

A shear test is designed to apply stress to a test sample so that it experiences a sliding failure along a plane that is parallel to the forces applied. Generally, shear forces cause one surface of a material to move in one direction and the other surface to move in the opposite direction so that the material is stressed in a sliding motion. Shear tests differ from tension and compression tests in that the forces applied are parallel to the two contact surface, whereas, in tension and compression they are perpendicular to the contact surfaces.

The procedure proposed to determine the shear resistance has been based on the Luong M.P. Shear Test [18]. This Test consist in a circular tube of axis $z = 0$ subjected, on its internal and external faces, to a shear stress parallel to $z = 0$ (see Fig. 4.17). The height of the notch is 10 mm whereas the width is 4 mm. On the internal tube has been applied a constant vertical velocity of 1 mm/s until failure.

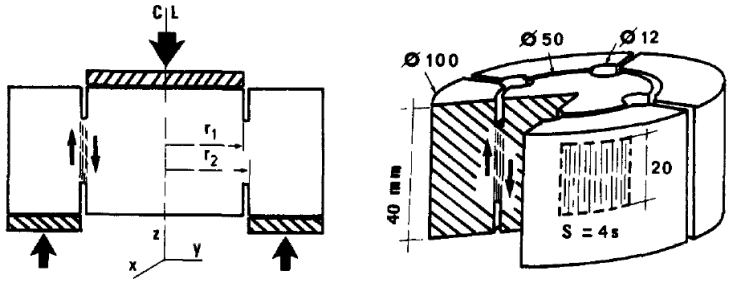

Figure 4.17: Geometry of the shearing zone of the direct shear test specimen [18]

The finite element model can be seen in the Fig. 4.18 and the meshes are depicted in the Fig. 4.19. As can be seen in the previous figures, the shear plane has been discretized with 4 finite elements in order to caption properly the stress gradient in this zone. The material properties of the sample are described in the table 4.4.

The damaged geometry of the sample and the discrete elements generated are shown in the Figs. 4.20 and ST2. In these figures one can see that the shear planes have been fully damaged up to the failure of the sample. This effect is relfected in the Fig. 4.23, where there is an initial elastic branch until the first DEM are generated. In that moment, the stiffness of the specimen decreases and, in the same manner, the slope of the Displacement-Reaction curve. Finally, knowing that the shear planes have a total area of $4 * 0.00044m^2$, and extracting the maximum applied load on the sample, one can compute the stress level achieved whose value is 5.10 MPa. In general the shear strength of the concrete is approximately 1/5 or 1/6 of the compressive stress as can be seen in [18]. According to the previous statement, the obtained result is coherent and, indeed, very accurate. If we observe the Fig. 4.22, one can see that the crack path obtained in the laboratory is similar to the one obtained in the numerical simulation. As expected, the 4 shear planes are completely damaged and a solid cylinder can be extracted from de specimen.

Parameter	Value
Young's modulus (E)	35000 MPa
Poisson's ratio (ν)	0.22
Compressive strength (σ_c)	30 MPa
Tensile strength (σ_t)	3 MPa
Fracture energy (G_f)	75 J/m^2

Table 4.4: Material properties used in the shear test

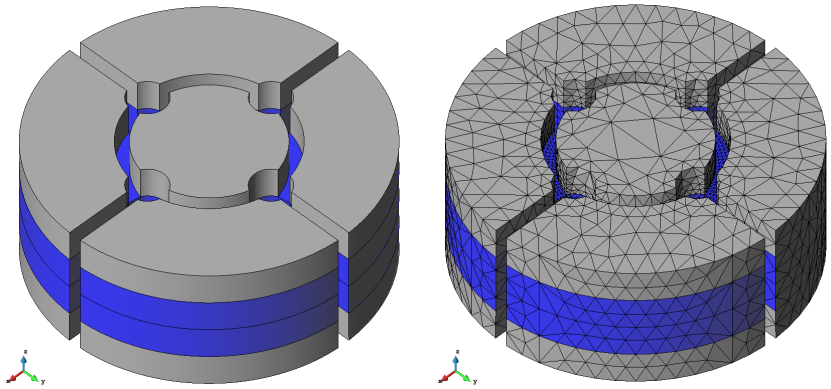

Figure 4.18: Finite element model and mesh used in the Shear Test with 87176 elements

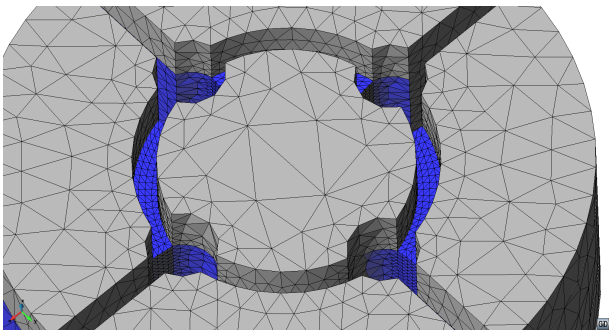

Figure 4.19: Detail of the mesh in the shear planes

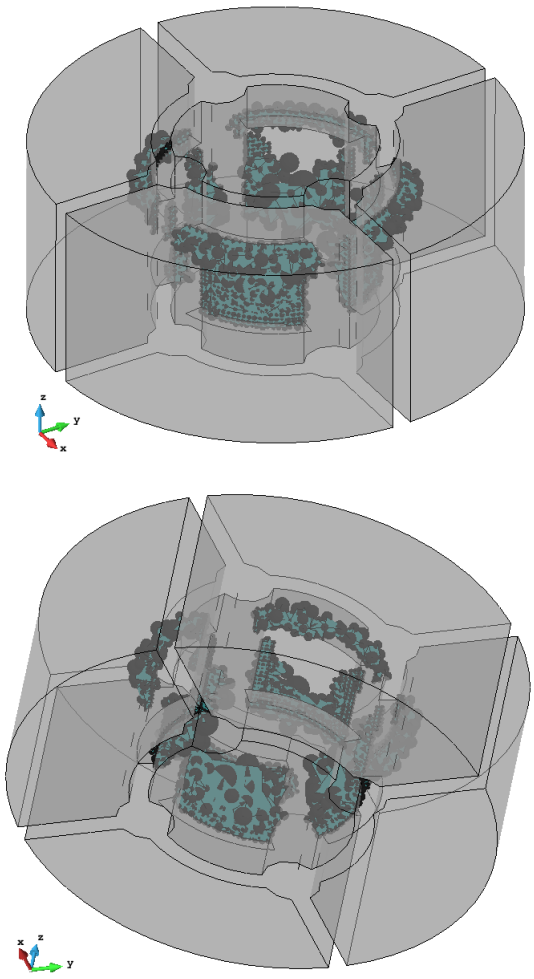

Figure 4.20: Damaged gometry and DEM generated (view 1 and 2)

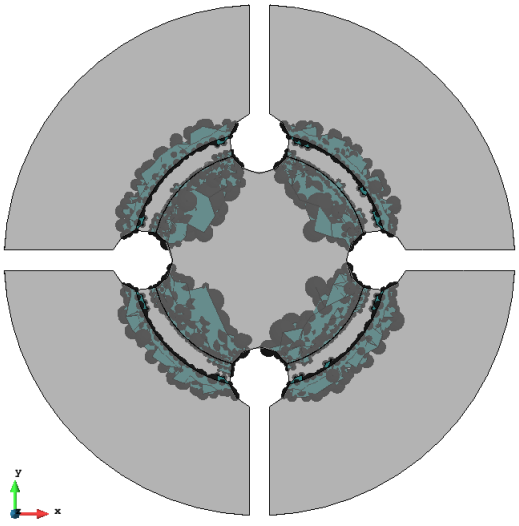

Figure 4.21: Damaged gometry and DEM generated (view 3)

Figure 4.22: Damaged samples analysed in the laboratory

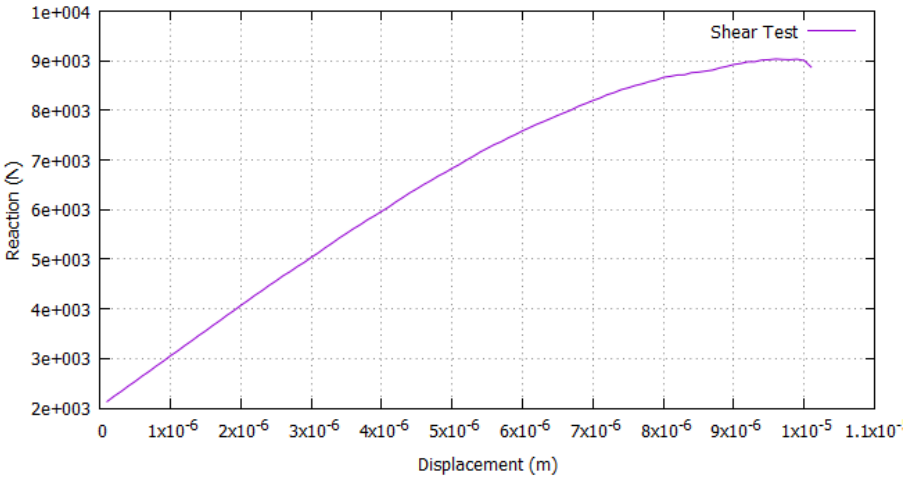

Figure 4.23: Displacement-Reaction evolution

4.3.4 Tensile Test

Tensile testing, is also known as tension testing, is a fundamental materials science test in which a sample is subjected to a controlled tension until failure. This example corresponds to the fracture analysis of a normalized concrete sample under tensile stress.

A tensile specimen is a standardized sample cross-section [11]. It has two shoulders and a gage (section) in between. The shoulders are large so they can be readily gripped, whereas the gauge section has a smaller cross-section so that the deformation and failure can occur in this area. In the Fig. 4.24 the geometry is defined as well as the three control points whose evolution is analysed.

The study has been performed using the 2D FEM-DEM technique previously described. In order to localize the fracture, only one band of elements is allowed to break at the failure stress level corresponding to the tested material. The constant imposed velocity at the tip of the sample is $0.5 \cdot 10^{-6}$m/s.

If one extract the maximum load ($P = 0.522N$) applied to the sample and divide it by the surface of the failure section ($S = 5.2 \cdot 10^{-5} m^2$) one obtain a peak stress level equal to 10.038 kPa which is very close to the analytical value shown in the table 4.5.

The properties of the material used in the specimen are specified in the table 4.5. In the Fig. 4.26 can be seen that the sample breaks in the center zone, where the discrete elements are localized.

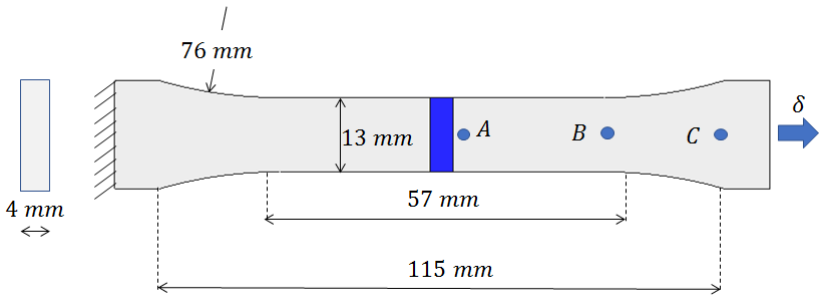

Figure 4.24: Tensile test sample geometry

Parameter	Value
Young's modulus (E)	30000 MPa
Poisson's ratio (ν)	0.2
Compressive strength (σ_c)	10 MPa
Tensile strength (σ_t)	10 kPa
Fracture energy (G_f)	$0.75 \cdot 10^4 J/m^2$

Table 4.5: Material properties used in the 3D simulations

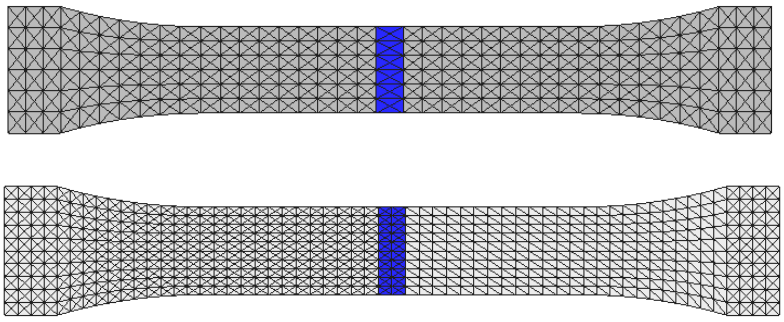

Figure 4.25: Finite Element meshes used in the simulations of the tensile test with 5616 and 29760 tetrahedral elements, respectively

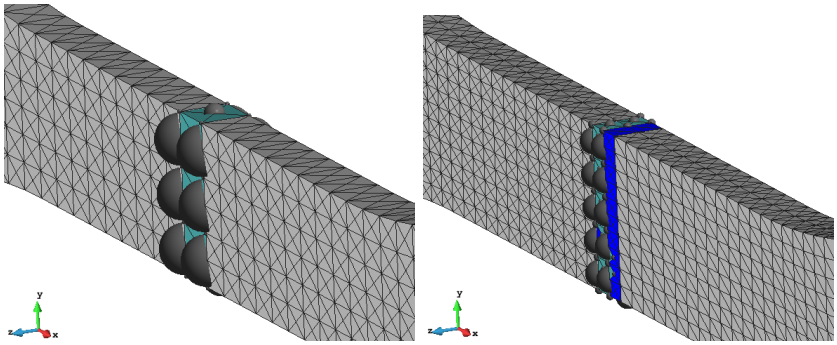

Figure 4.26: Damaged geometry and the discrete elements generated

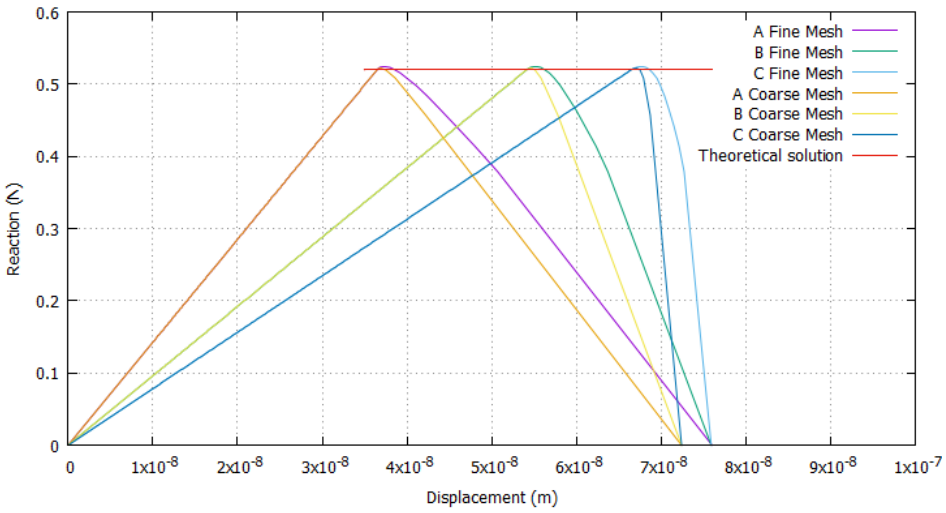

Figure 4.27: Force-Displacement evolution for the two analysed meshes in each control points A,B and C

As shown in the Fig. 4.27, the elastic branch is similar and does not depend on the mesh refinement. On the other hand, once the crack initiates, the displacement of the control points is ruled by the elastic energy stored in the specimen which, in this case, depends on the element size.

4.3.5 Tunnel Portal Subjected to Internal Blast Loading

In this section the behaviour of an underground structure subject to blast action is studied. As is usually done in mining industry, the blasts are positioned and detonated with a certain delay in order to excavate more efficiently. The geometry of the tunnel portal can be seen in the Fig. 4.29. Since this is an underground tunnel, there must be some earth pressures acting on the edges of the previous geometry, this means that one must initially compress the surface of the model in order to simulate the earth pressures as depicts the Fig. 4.30. The blast loading can be represented by a uniform pressure whose temporal evolution is displayed in the Fig. 4.28.

The finite element mesh is shown in the Fig. 4.32 and the results of the damaged geometry and the discrete elements generated are displayed in the Fig. 4.33. As can be seen in the Fig. 4.33, the rock of the tunnel portal has been disaggregated due to the blast loading in a realistic way. It is important to note that before obtaining the previous result, some iterative procedure has been conducted consisting in varying the delays between the blasts and the maximum pressures of them until an efficient blasting was obtained. This means that, one can predefine a certain order and temporization of the detonations and simulate its effect without any experimental test. This fact is the most important and promising advantage of the FEM-DEM formulation in the mining industry for instance.

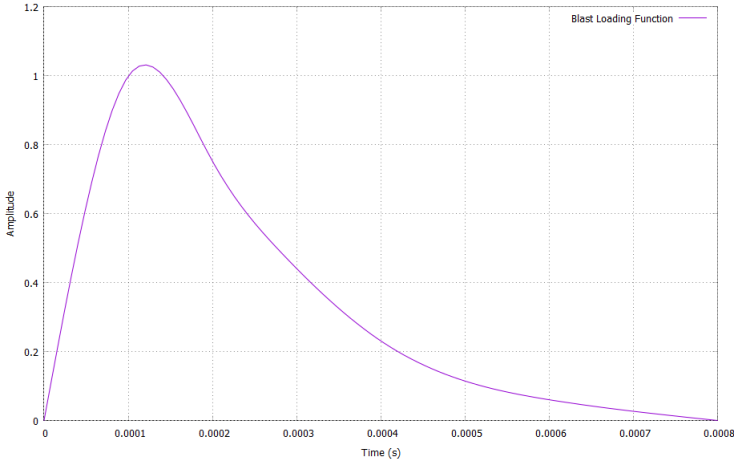

Figure 4.28: Blast loading amplitude function

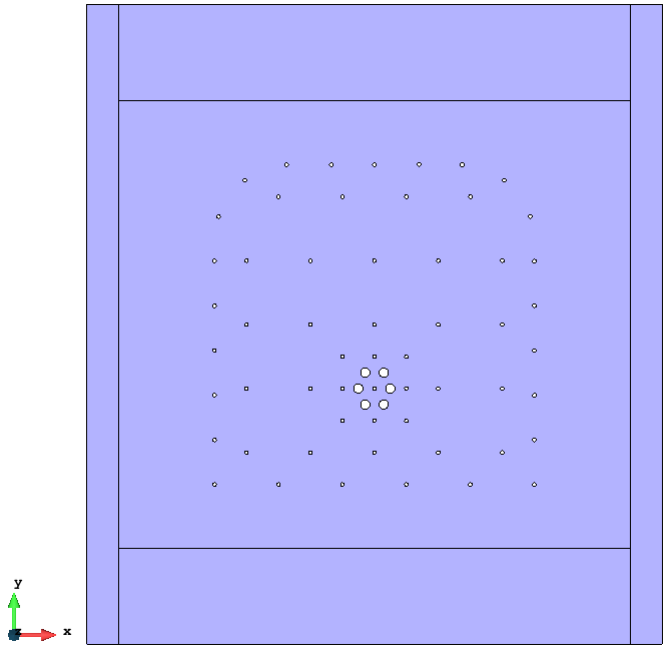

Figure 4.29: Tunnel portal geometry

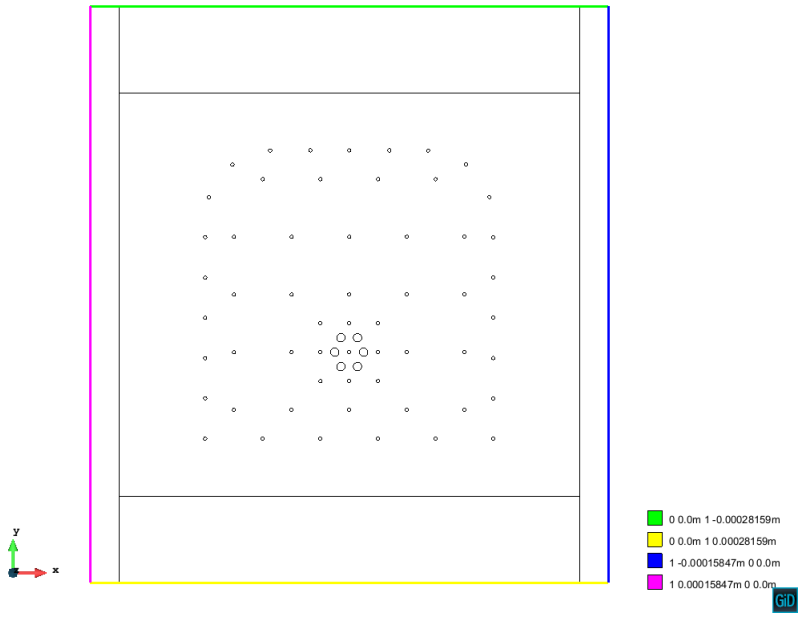

Figure 4.30: Tunnel portal boundary conditions

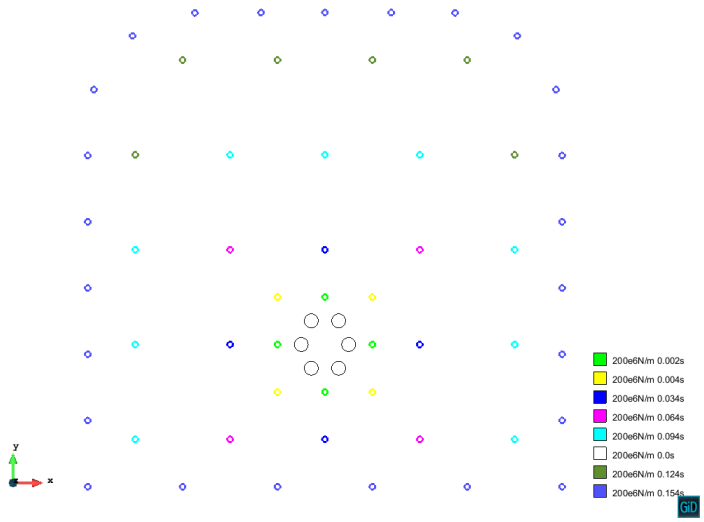

Figure 4.31: Tunnel portal applied blast loads

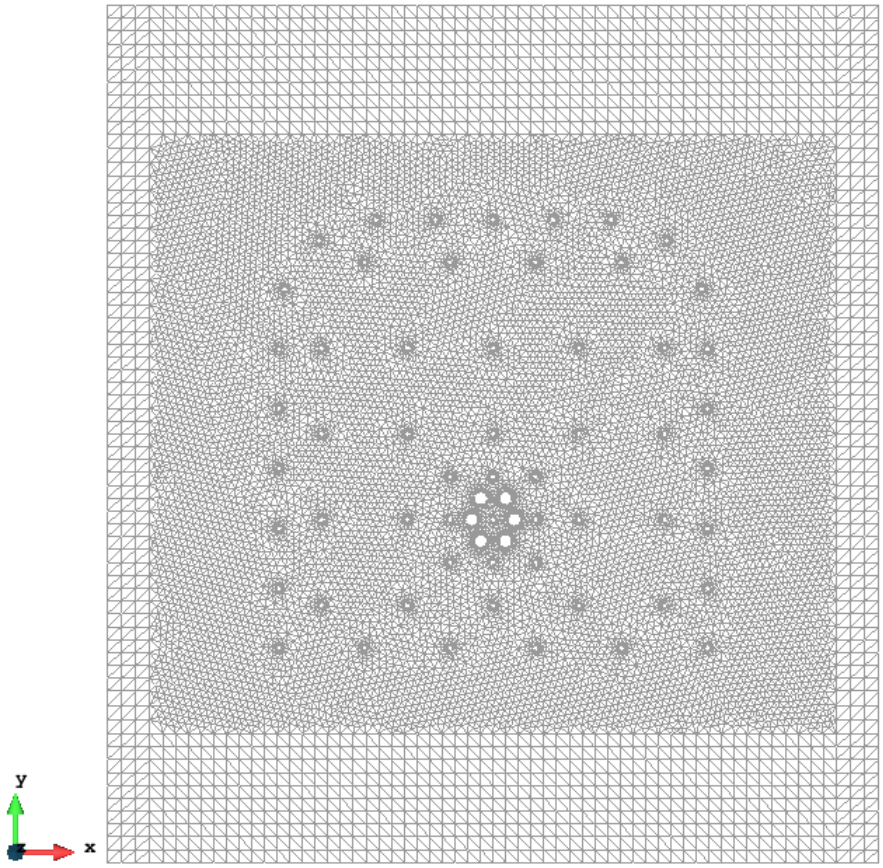

Figure 4.32: Finite element mesh of the tunnel with 25189 triangular elements

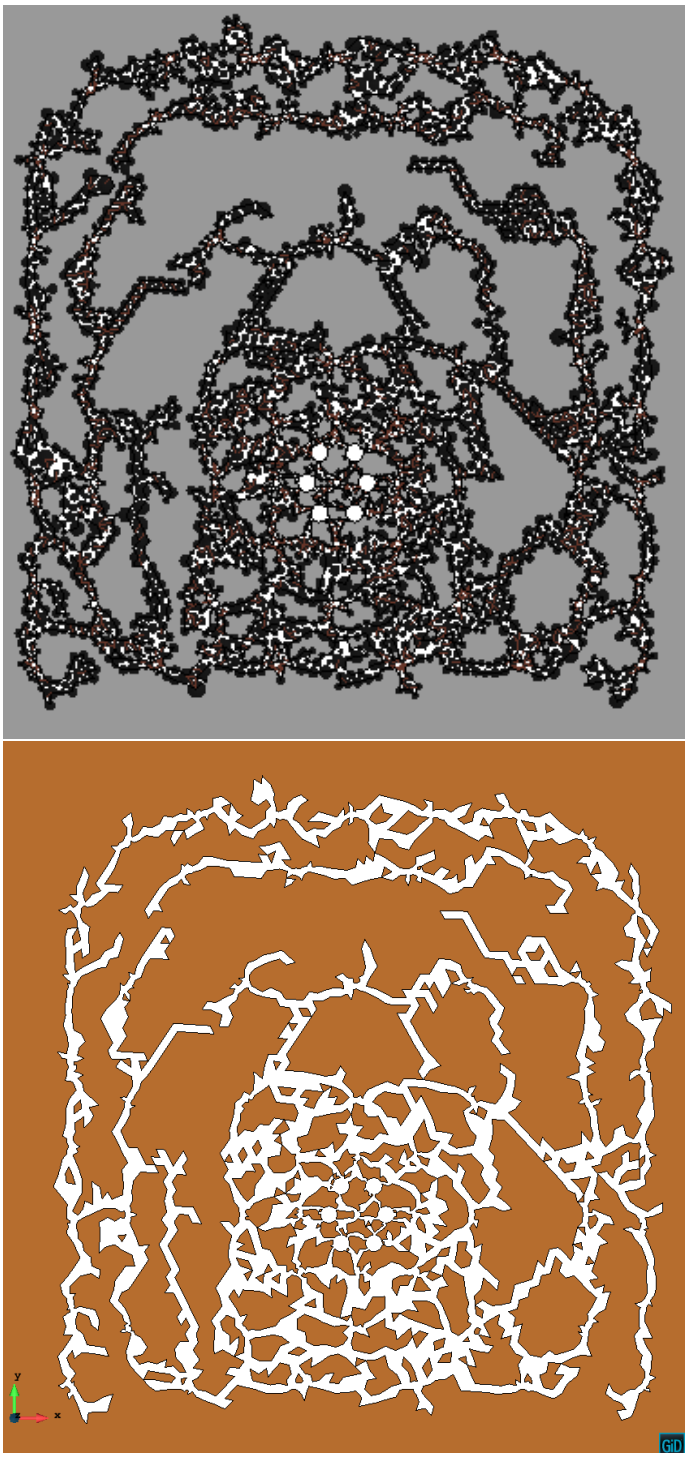

Figure 4.33: Damaged geometry and discrete elements generated

Parameter	Value
Young's modulus (E)	20000 MPa
Poisson's ratio (ν)	0.23
Compressive strength (σ_c)	20 MPa
Tensile strength (σ_t)	5 MPa
Fracture energy (G_f)	200 J/m^2

Table 4.6: Filling material properties

4.3.6 Masonry Arch Submitted to a Differential Settlement

In this section, the effect of a differential settlement on a masonry arch is studied. Differential or uneven settlement occurs when the soil beneath a structure can not bear the weight imposed. The settlement of a structure is the amount that the structure will "sink" during and after construction. Differential settlements become a big problem when the foundation settles unevenly. The more uneven the settlement is, the greater the problems are to the structure.

As can be seen in the Fig. 4.34, the arch is composed by two materials: the filling material is a soft soil that covers the arch and, on the other hand, the masonry material is an stiffer material that behaves in a brittle manner. In the same figure is schematically described the way that the differential settlement (δ) is applied in one of the supports whereas the other support is fixed. The mechanical properties of the materials are described in the tables 4.6 and 4.7.

In the Fig. 4.36 one can observe the deformed geometry and the crack path obtained as well as the discrete elements generated. Note that the damaged elements are, when it is possible, localized in the soft material because its Young's modulus is lower and, consequently, the strain is greater. The deformed geometry showed in the Fig. 4.36 corresponds to a vertical displacement in the right suport of $\delta = 0.233m$.

In the Fig. 4.35 is plotted the vertical stress path. In this figure can be see that the left support is still compressed. In addition, note the stress concentration in the end of the crack lips advancing through the filling material.

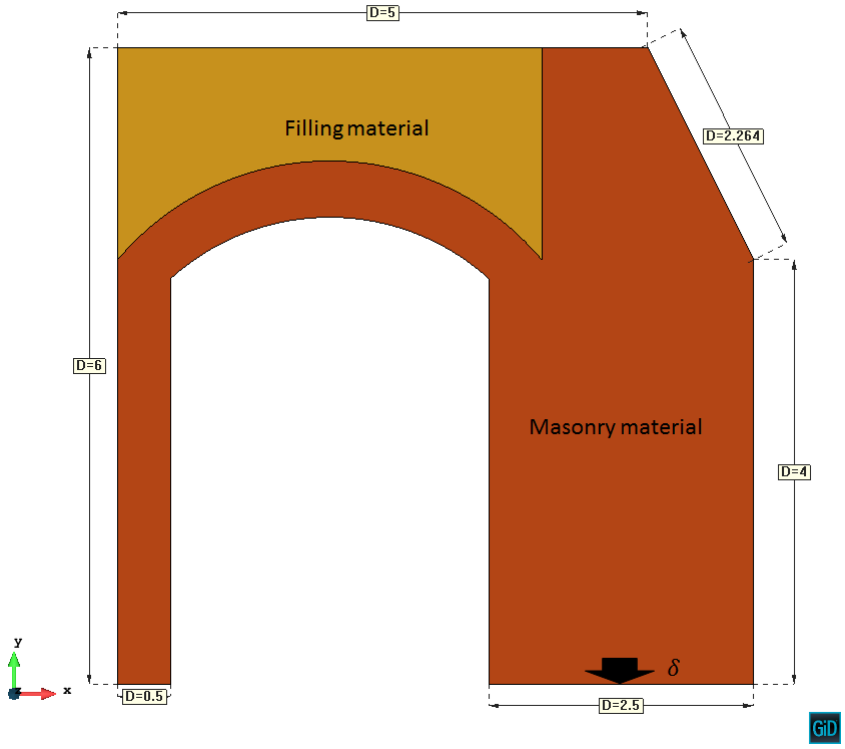

Figure 4.34: Masonry arch geometry

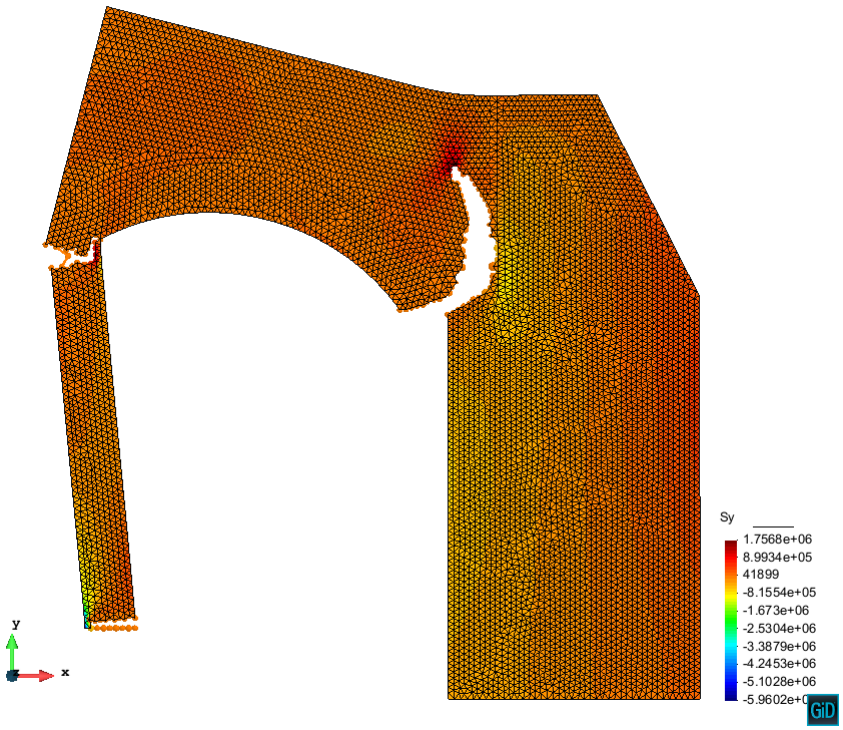

Figure 4.35: Vertical stress path

Parameter	**Value**
Young's modulus (E)	30000 MPa
Poisson's ratio (ν)	0.25
Compressive strength (σ_c)	20 MPa
Tensile strength (σ_t)	5 MPa
Fracture energy (G_f)	200 J/m^2

Table 4.7: Masonry material properties

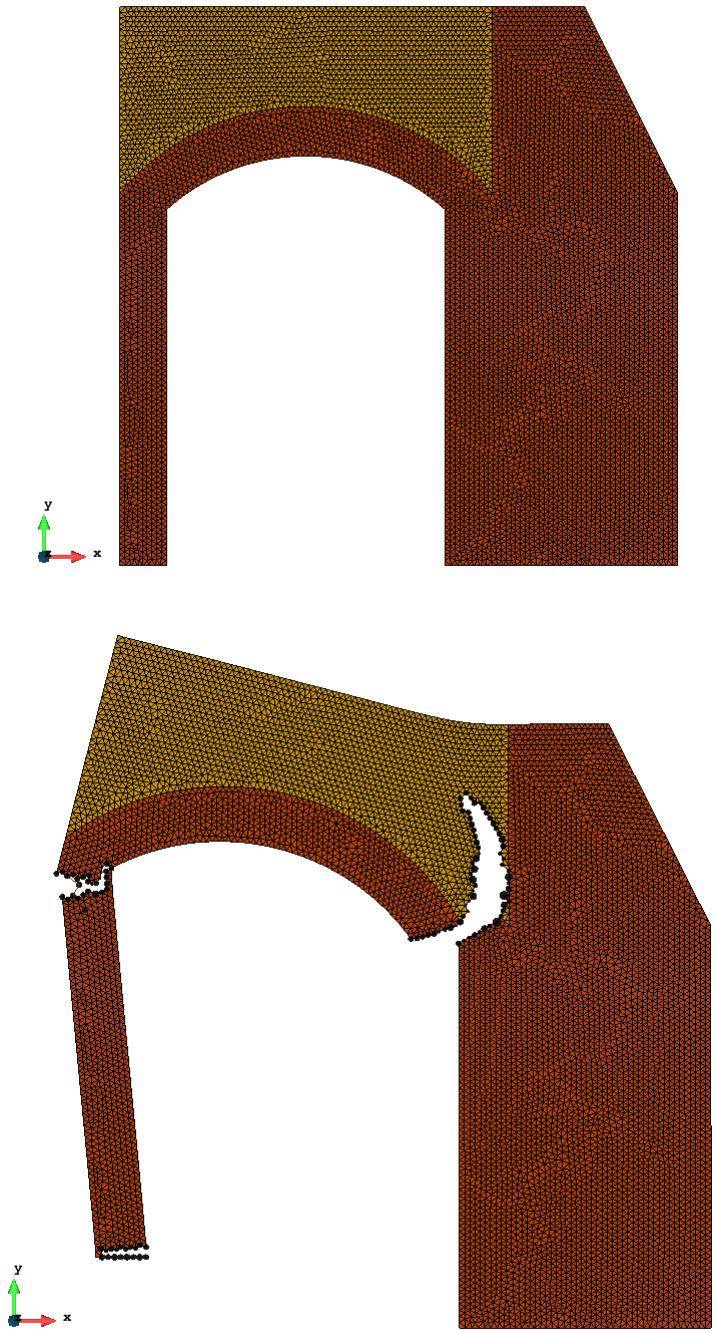

Figure 4.36: Finite element mesh with 14118 triangular elements and the damaged geometry (amplified x3.5)

Parameter	Value
Young's modulus (E)	35000 MPa
Poisson's ratio (ν)	0.22
Compressive strength (σ_c)	30 MPa
Tensile strength (σ_t)	2 MPa
Fracture energy (G_f)	100 J/m^2

Table 4.8: Aqueduct material properties

4.3.7 Roman aqueduct

In this section an ancient Roman aqueduct has been simulated. For instance, the geometry of the aqueduct is identical to the Pont du Gard which is an ancient Roman aqueduct that crosses the Gardon River near the town of Vers-Pont-du-Gard in southern France. The geometry of the model can be seen in the Fig. 4.38. The aqueduct has a total length of 275 m and a width of 6.4 m with a maximum height of 48.8 m. The finite element mesh composed of 44493 linear triangles can be seen in the Figs. 4.39 and 4.40.

The structure has been simulated with a 2D plane stress formulation considering the real width of it. The aqueduct has been submitted to an incremental uniform load on the top of it up to failure. The material properties of the aqueduct can be analysed in the table 4.8.

The firsts sections to fail are the closest to the ends of the aqueduct. In the Figs. 4.41 and 4.42 one can see that one of the pillars have failed and they have no resistance so, it is evident that locally the structure has failed but can absorb more energy. If the vertical load keeps increasing, one can observe that the central part of the aqueduct is the one that copes with the load until it fails. At this moment some of the pillars have failed (see Fig. 4.43) and the whole structure collapses.

In this example one can see the high potential of the FEM-DEM formulation in risk assessment of structures and in the prediction of failure mechanisms which are, in general cases, difficult to deal with in complex structures such as the one studied in this case.

Figure 4.37: Picture of the Roman aqueduct analysed

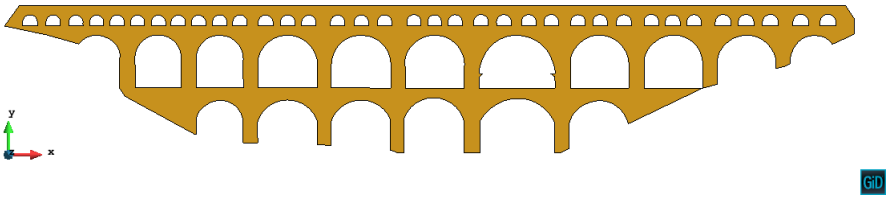

Figure 4.38: Finite element model of the aqueduct

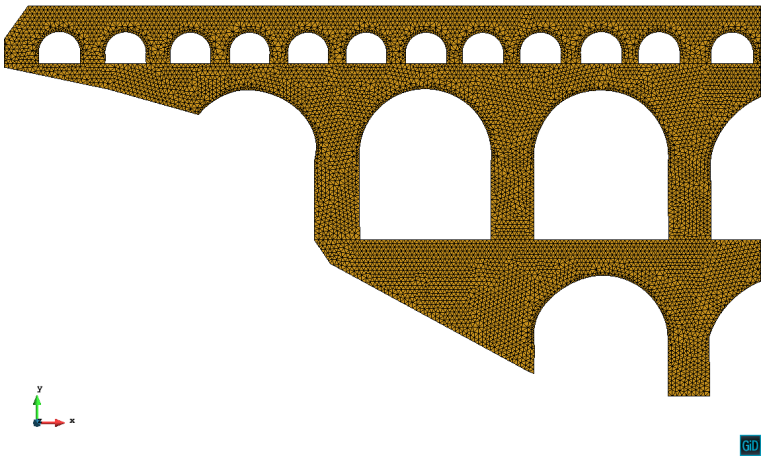

Figure 4.39: Finite element mesh (view 1)

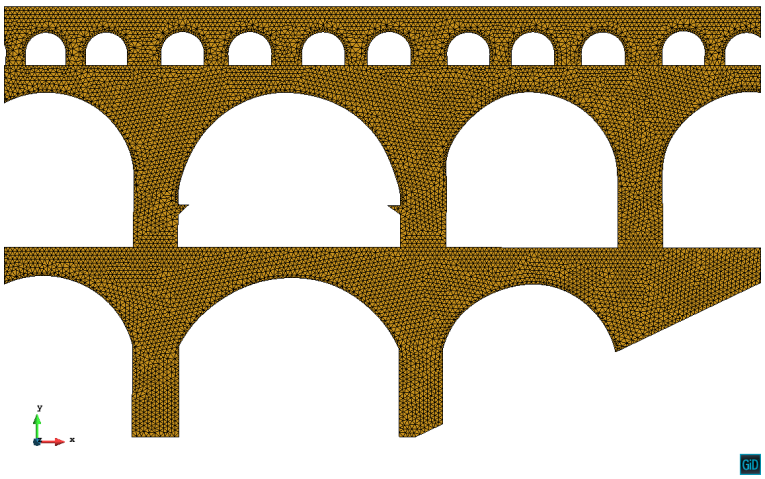

Figure 4.40: Finite element mesh (view 2)

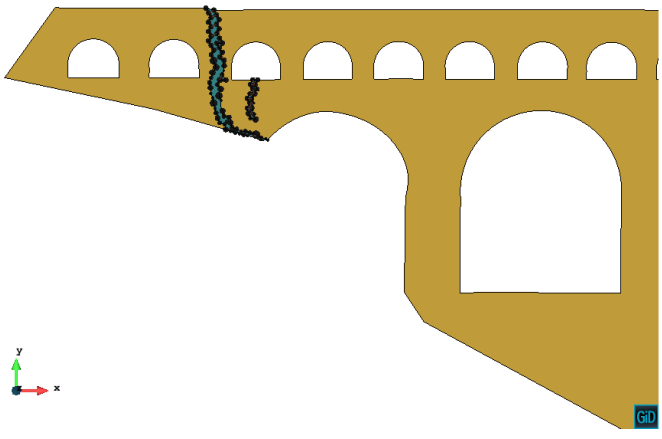

Figure 4.41: First stage damaged section, left side of the aqueduct

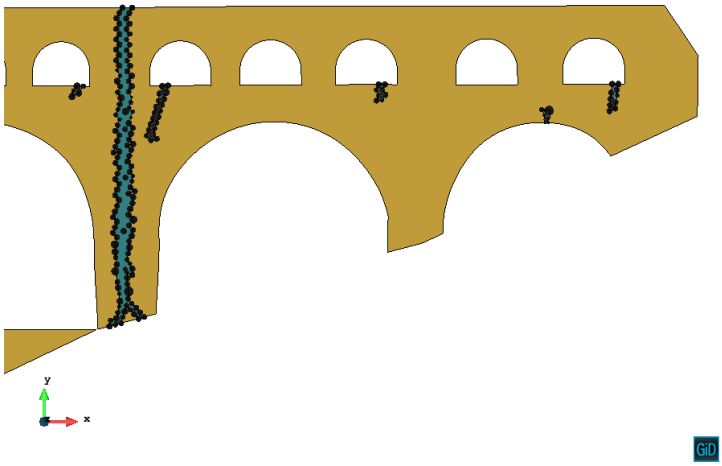

Figure 4.42: First stage damaged section, right side of the aqueduct

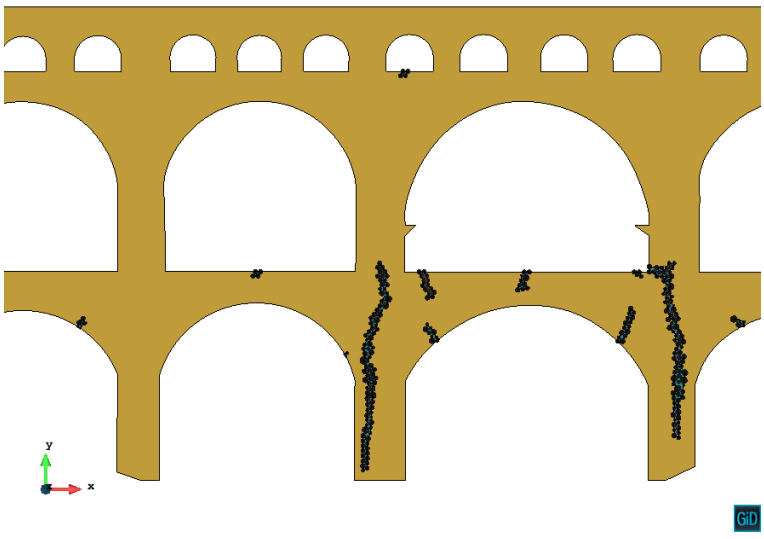

Figure 4.43: Second stage damaged section,central part of the aqueduct

Chapter 5

Conclusions and Future Research Lines

After a long period of calculations and study of the damage models and the FEM-DEM formulation in the seek of a numerical method capable of predicting the onset and evolution of crack paths in frictional materials, some conclusions can be drawn.

First, after performing the indirect tensile (BTS), uni-axial compression (UC) and the tensile tests, one can see that the formulation is capable of simulating the crack path in a realistic way and, quantitatively, obtaining accurate results in terms of maximum allowable load. Additionally, the stress-strain evolution obtained with the FEM-DEM formulation is coherent with the expected results as well as comparing with the classical damage models.

Another important fact is that the failure criterion is considered at the mid-point of the element sides using a smooth stress field which does not need any additional considerations such as stabilization, or complex mixed finite element formulations. This means that the implementation of this formulation is quite simple and has yielded, as stated before, promising results, both qualitative and quantitative. The mentioned smoothed stress field also reduces the mesh sensitiveness as seen in the BTS, UC and tensile tests in which the mesh does not affect significantly the final crack path.

Concerning the civil engineering and mining industry, after analyzing the results

of the tunnel portal and the masonry arch has been proved that the FEM-DEM formulation has a promising future in the blast loading simulations with the objective of enhance the effectiveness of the excavation. With the FEM-DEM formulation one can simulate the detonation varying the position and the delays between the explosives as well as the explosive quantities. In this way one can predict the effect of the blast loading by knowing the material properties of the soil without any additional cost.

Thereby, in the near future there are various aspects on the current formulation that could be implemented in order to apply this method in other fields. For instance, a coupled formulation using the FEM-DEM and the Fluid Mechanics can offer a wide range of applications such as the *Fracking* technology, which is the process of creating fractures in rocks and rock formations by injecting specialized fluid into cracks to force them to open further. In this case the FEM-DEM formulation can predict the evolution of the crack path whereas the fluid mechanics formulation analyses the fluid pressures and the interaction solid-fluid.

Another option would consist in simulate the damage process of *Seawalls*, which are a form of coastal defence constructed where the sea, and associated coastal processes, impact directly upon the landforms of the coast. The purpose of a sea wall is to protect areas of human habitation, conservation and leisure activities from the action of tides, waves, or tsunamis. As stated before, one could simulate the effect of a wave (fluid pressure) impacting on a seawall and perform a risk assessment.

Additionally, a mesh adaptative technique could be implemented in order to improve the mesh refinement adapting the element size to the stress level. This technique would generate a finer mesh where the crack path appears and, in this way, one could obtain a narrower crack path while the total number of elements is not excessively increased comparing to the initial mesh.

References

[1] Z. Bazant and J. Planas. Fracture and size effect in concrete and other quasibrittle materials. *CRC Press*, page 640, 1997. [Cited in pages 58 and 62]

[2] F. Carneiro. A new method to determine the tensile strength of concrete. *In Proceedings of the 5th meeting of the Brazilian Association for Technical Rules*, pages 126–129. [Cited in page 54]

[3] M. Cervera, M. Chiumenti, and R. Codina. Mixed stabilized finite element methods in nonlinear solid mechanics. part ii: Strain localization. *Comput Methods Appl Mech Eng*, 199:2571–2589, 2004. [Cited in page 49]

[4] M. Cervera, M. Chiumenti, and R. Codina. Mesh objective modelling of cracks using continuous linear strain and displacements interpolations. *Int J Numer Methods Eng*, 87:962–987, 2011. [Cited in page 1]

[5] M. Cervera, M. Chiumenti, and C. A. de Saracíbar. Shear band localization via local j2 continuum damage mechanics. *Comput Methods Appl Mech Eng*, 193:849–880, 2004. [Cited in pages 49 and 52]

[6] P. Cundall and D. Strack. A discrete numerical model for granular assemblies. *Geotechnique*, 1979. [Cited in pages 45, 46, and 48]

[7] P. Cundall and O. Strack. A discrete numerical model for granular assemblies. *Geotechnique*, 29(1):45–65, 1979. [Cited in page 1]

[8] R. Faria, J. oliver, and M. Cervera. A strain-based plastic viscous-damage model for massive concrete structures. *Int J Solids Structures*, 35(14):1533–1558, 1998. [Cited in page 49]

[9] D. Hayhurst. Creep rupture under multi-axial states of stress. *Journal of the Mechanics and Physics of Solids*, 20(6):381–382, 1972. [Cited in page 27]

[10] R. Idelsohn and E. Oñate. Finite volumes and finite elements: Two good friends. *Int J Numer Methods Eng*, 37(19):3323–3341, 1994. [Cited in page 1]

[11] A. International. *Standard test method for tensile properties of plastics.* Conshohocken, 2003. [Cited in page 70]

[12] L. Kachanov. *On the time of fracture under conditions of creep.* Izv. AN SSSR, Nauk, 1958. [Cited in page 27]

[13] S. Katagiri and S. Takada. Development of fem-dem combined method for fracture analysis of a continuos media. *emoirs of the Graduate School of Science and Technology, Kobe University Japan*, 20A:65–79, 2003. [Cited in pages 1 and 49]

[14] C. Labra and E. Oñate. High-density sphere packing for discrete element method simulations. *Commun Numer Meth Engng*, 25(7):837–849, 2009. [Cited in page 1]

[15] F. Leckie and D. Hayhurst. Creep rupture of structures. *Proceedings of the Royal Society of London. A. Mathematical and Physical Sciences*, 340(1622):323–347, 1974. [Cited in page 27]

[16] J. Lemaitre and J. Chaboche. *Mécanique des matériaux solides.* Dunod, Paris, 1985. [Cited in page 27]

[17] J. Lopez, S. Oller, E. Oñate, and J. Lubliner. A homogeneous constitutive model for masonry. *Int J Numer Meth Engng*, 46:16511671, 1999. [Cited in page 52]

[18] M. Luong. Tensile and shear strengths fo concrete and rock. *Engineering Fracture Mechanics*, 35:127–135, 1990. [Cited in pages X, 62, 65, and 66]

[19] J. Mazars. A description of micro-and macroscale damage of concrete structures. *Engineering Fracture Mechanics*, 25(5):729–737, 1986. [Cited in page 27]

[20] J. Mazars and G. Pijaudier-Cabot. From damage to fracture mechanics and conversely: a combined approach. *International Journal of Solids and Structures*, 33(20):3327–3342, 1996. [Cited in page 27]

[21] J. Mishnaevsky, N. Lippmann, and S. Schmauder. Computational modelling of crack propagation in real microstructures of steels and virtual testing of artidicially designed materials. *International Journal of Fracture*, 120:581–600, 2003. [Cited in page 1]

[22] A. Munjiza. *The combined finite-discrete element method.* ISBN 0-470-84199-0, Wiley, 2004. [Cited in pages 1 and 49]

[23] E. Oñate. *Cálculo de estructuras por el método de elementos finitos: Análisis elástico lineal.* Centro Internacional de Métodos Numéricos en Ingeniería, Barcelona, 1992. [Cited in pages IX, 6, 7, 9, 12, 14, 16, 17, 18, 21, and 25]

[24] E. Oñate and J. Rojek. Combination of discrete element and finite element methods for dynamic analysis of geomechanics problems. *Comput Meth Appl Mech Engrg*, 193:3087–3128, 2004. [Cited in page 1]

[25] E. Oñate and J. Rojek. Multiscale analysis using a coupled discrete/finite element method. *Interaction and Multiscale Mechanics: An International Journal*, 1(1):1–31, 2007. [Cited in page 1]

[26] E. Oñate, J. Rojek, and C. Labra. Discrete element simulation of rock cutting. *Int J of Rock Mechanics and Mining Sciences*, 48:1010, 2011. [Cited in page 1]

[27] E. Oñate, J. Rojek, F. Zárate, and J. Miquel. Modelling of rock, soil and granular materials using spherical elements. *2nd European Conference on Computational Mechanics ECCM-2001*, 2001. [Cited in page 1]

[28] E. Oñate, F. Zárate, J. Miquel, M. Santasusana, M. Celigueta, and F. Arrufat. A local constitutive model for the discrete element method. application to geomaterials and concrete. *Computational Particle Mechanics*, 2(2):139–160, 2015. [Cited in pages IX, 1, 46, and 53]

[29] J. Oliver, M. Cervera, S. Oller, and J. Lubliner. Isotropic damage models and smeared crack analysis of concrete. *In Second international conference on computer aided analysis and design of concrete structures*, 2:945–958, 1990. [Cited in page 43]

[30] S. Oller. *Dinámica no lineal.* Centro Internacional de Métodos Numéricos en Ingeniería, Barcelona, 2001. [Cited in pages IX, 35, 36, 38, 39, 40, 42, and 43]

[31] S. Oller, S. Botello, J. Miquel, and E. Oñate. An anisotropic elastoplastic model based on an isotropic formulation. *Engineering Computations*, 12(3):245–262, 1995. [Cited in page 52]

[32] S. Oller, E. Oñate, J. Oliver, and J. Lubliner. Finite element nonlinear analysis of concrete structures using a "plastic-damage mode. *Engineering Fracture Mechanics*, 35(1):219–231, 1990. [Cited in page 27]

[33] Y. Rabotnov. Damage from creep. *Zhurn. Prikl. Mekh. Tekhn. Phys*, 2:113–123, 1963. [Cited in page 27]

[34] S. Shmauder, J. Wulf, and H. Fischmeister. Finite element modelling of crack propagation in ductile fracture. *Computation Materials Science*, 1:297–301, 1993. [Cited in pages 1 and 49]

[35] J. Simo and J. Ju. Strain-and stress-based continuum damage models-i. formulation. *International Journal of Solids and Structures*, 23(7):821–840, 1987. [Cited in page 27]

[36] S. Timoshenko and J. Goodier. *Theory of elasticity.* New York, 1951. [Cited in pages 6 and 8]

[37] J. Williams and R. O'Connor. Discrete element simulation and contact problem. *Arch ComputMethods Eng*, 6(4):279–304, 1999. [Cited in page 1]

[38] F. Zárate and E. Oñate. *A three dimensional FEM-DEM technique for predicting the evolution of fracture in geomaterials and concrete.* Research Report CIMNE PI410, Barcelona, 2015. [Cited in pages IX, 50, 51, 52, and 53]